Geol. Mag. **155** (*6*), *2018, pp. 1205–1229.* © *Cambridge University Press 2017*
doi:10.1017/S0016756816001357

Rare metals on shatter cone surfaces from the Steinheim Basin (SW Germany) – remnants of the impacting body?

E. BUCHNER*‡† & M. SCHMIEDER§¶

*HNU – Neu-Ulm University, Wileystraße 1, D-89231 Neu-Ulm, Germany
‡Institut für Mineralogie und Kristallchemie, Universität Stuttgart, Azenbergstraße 18, D-70174 Stuttgart, Germany
§USRA – Lunar and Planetary Institute, 3600 Bay Area Boulevard, Houston TX 77058, USA
¶NASA–SSERVI

(*Received* 16 May 2016; *accepted* 13 December 2016; *first published online* 13 February 2017)

Abstract – The ∼ 3.8 km Steinheim Basin in SW Germany is a well-preserved complex impact structure characterized by a prominent central uplift and well-developed shatter cones that occur in different shocked target lithologies. Scanning electron microscopy coupled with energy-dispersive X-ray spectroscopy and electron probe microanalysis have revealed, for the first time, the occurrence of rare metals on the Steinheim shatter cone surfaces. Shatter cones produced from the Middle Jurassic (Aalenian) Opalinus Claystone ('Opalinuston'), temporarily exposed in the central uplift in spring 2010, and shatter cones in Upper Jurassic (Oxfordian) limestones from the southeastern crater rim domain are commonly covered by faint coatings. The Opalinus Claystone shatter cone surfaces carry coatings dominated by Fe, Ca, P, S and Al, and are covered by abundant small, finely dispersed microparticles and aggregates of native gold, as well as locally elevated concentrations of Pt. On several surfaces of the claystone shatter cones, additional Fe, Ni and Co was detected. The Ca–Mn-rich coatings on the limestone shatter cone surfaces locally include patches of Fe, Ni, Co, Cu and Au in variable amounts and proportions. The intriguing coatings on the Steinheim shatter cones could either stem from the impacted Lower Jurassic to Palaeogene sedimentary target rocks; from the crystalline-metamorphic Variscan crater basement; or, alternatively, these coatings might represent altered meteoritic matter from the Steinheim impactor, possibly an iron meteorite, which may have been remobilized during post-impact hydrothermal activity. We here discuss the most plausible source for the rare metals found adherent to the shatter cone surfaces.

Keywords: Steinheim, impact crater, shock metamorphism, shatter cones, meteorites

1. Introduction

Among a number of structural features suggestive of meteorite impact on Earth, shatter cones are the only macroscopic features currently accepted as evidence for shock metamorphism (e.g. French & Short, 1968; French, 1998; Langenhorst, 2002; French & Koeberl, 2010). First described at the Steinheim Basin (Baden-Württemberg, SW Germany; Figs 1, 2) by Branco & Fraas (1905) more than 100 years ago as the '*Steinheimer Strahlenkalke*', and still interpreted as of cryptovolcanic origin at that time, shatter cones were later recognized to be associated with – and restricted to – meteorite impact structures (e.g. French & Koeberl, 2010). Structurally and genetically, shatter cones are oblate, spoon-shaped to almost conical, or curvilinear fracture phenomena characterized by a distinct striation along the long ('cone') axis that is thought to form in response to rapid and dynamic tensile stresses during impact (e.g. Sagy, Reches & Fineberg, 2002; Sagy, Fineberg & Reches, 2004) by the interference of shock waves with target rocks at shock pressures in excess of ∼ 2 GPa (e.g. Baratoux & Melosh, 2003). Recent reviews of shatter cone formation are provided by, for example, Baratoux & Reimold (2016 and references therein) and Osinski & Ferrière (2016). Sizes of individual shatter cones may vary from some millimetres (e.g. this study) to >10 m (e.g. at the Slate Islands impact structure, Ontario, Canada; Sharpton *et al*. 1996; French, 1998). In the Steinheim Basin and many other smaller impact structures, shatter cones are known from rocks that form the crater floor of the impact structure. In the Steinheim Basin, well-developed shatter cones are known from Upper Jurassic limestones of the structural crater floor mainly from the southern and eastern part of the crater (e.g. Heizmann & Reiff, 2002). Schmieder & Buchner (2013), moreover, described morphologically variable shatter cones from concretions of the Middle Jurassic Opalinus Claystone that builds up the central domain of the central uplift.

Earlier studies by Gay (1976), Gay, Comins & Simpson (1978), Gibson & Spray (1998) and Nicolaysen & Reimold (1999) investigated the composition of exotic melting- and vaporization-related microfeatures (spherules, as well as melt splats and fibres) adherent to shatter cones from the large, eroded Vredefort impact structure in South Africa and the

†Author for correspondence: elmar.buchner@hs-neu-ulm.de

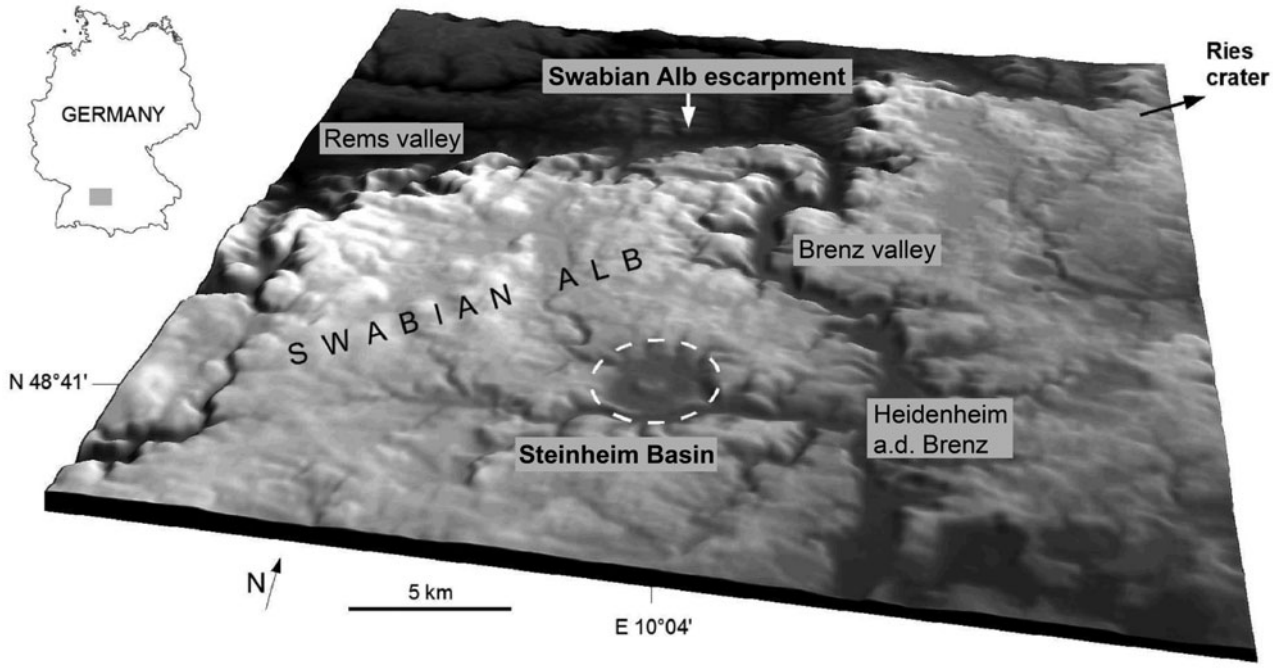

Figure 1. Shaded relief image of the eastern Swabian Alb plateau showing the position of the Steinheim Basin (dashed line indicates ~ 3.8 km crater diameter), the adjacent valleys, a main morphological feature – the Alb escarpment – and the position of the city of Heidenheim an der Brenz (see small map for position of the scene in SW Germany; Shuttle Radar Topography Mission data, 2-fold vertical exaggeration).

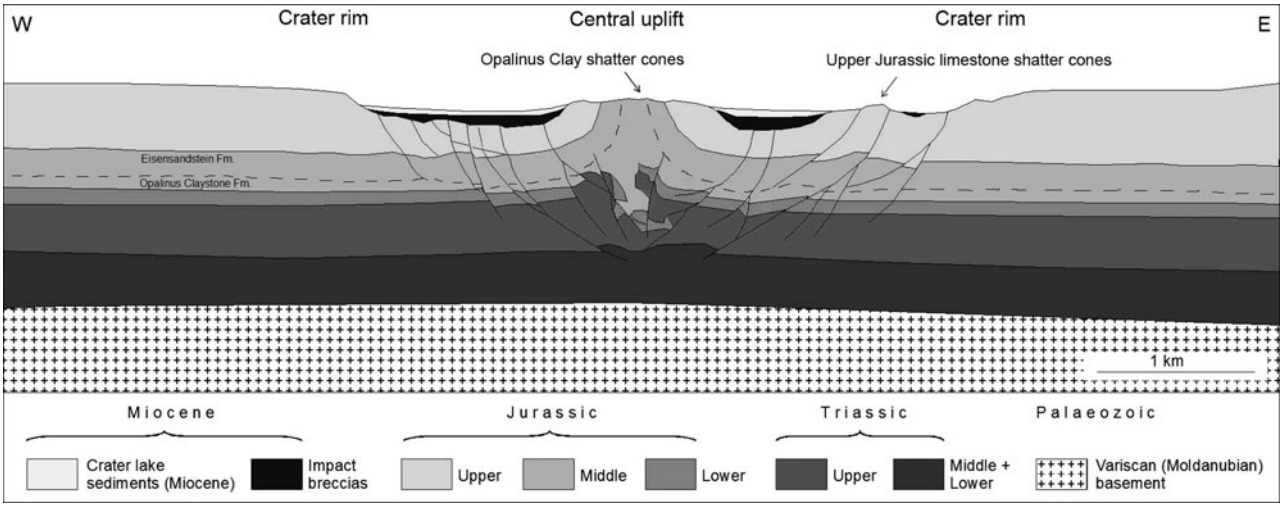

Figure 2. Schematic cross-section of the Steinheim Basin displaying the main sedimentary units of the Steinheim target rocks and the position of the Middle Jurassic 'Opalinus Clay' layer with the sampling locality of the Opalinus Claystone shatter cones on the top of the central uplift and of the Upper Jurassic limestone shatter cones in rocks forming the crater floor (modified from Schmieder & Buchner, 2013; after Mattmüller, 1994). Approximately 1.5-fold vertical exaggeration.

Sudbury Basin in Canada, respectively. A recent study by Schmieder *et al*. (2015) reported brecciated schreibersite and Fe–Ni oxide flakes on the surface of a limestone shatter cone from a recently identified impact site at Agoudal in Morocco (e.g. Lorenz *et al*. 2014; Schmieder *et al*. 2015). Similarly, microparticles of meteoritic affinity were recently detected on shatter cones from the structural crater floors of the Ries crater in Germany (Buchner & Schmieder, 2016*a*), the East Clearwater Lake impact structure in Québec, Canada (Buchner & Schmieder, 2016*b*; compare Grieve, Palme & Plant, 1980), and the Marquez Dome impact structure in Texas, USA (Schmieder & Buchner, 2016), respectively. The exotic particles adherent to the shatter cones are interpreted as possible impactor traces. Motivated by these findings, we here investigate shatter cones from concretions of the Middle Jurassic Opalinus Claystone sampled on the top of the Steinheim Basin central uplift, and shatter cones in Upper Jurassic limestones of the crater floor collected on fields inside the southeastern crater rim (see Figs 2, 3).

https://doi.org/10.1017/S0016756816001357 Published online by Cambridge University Press

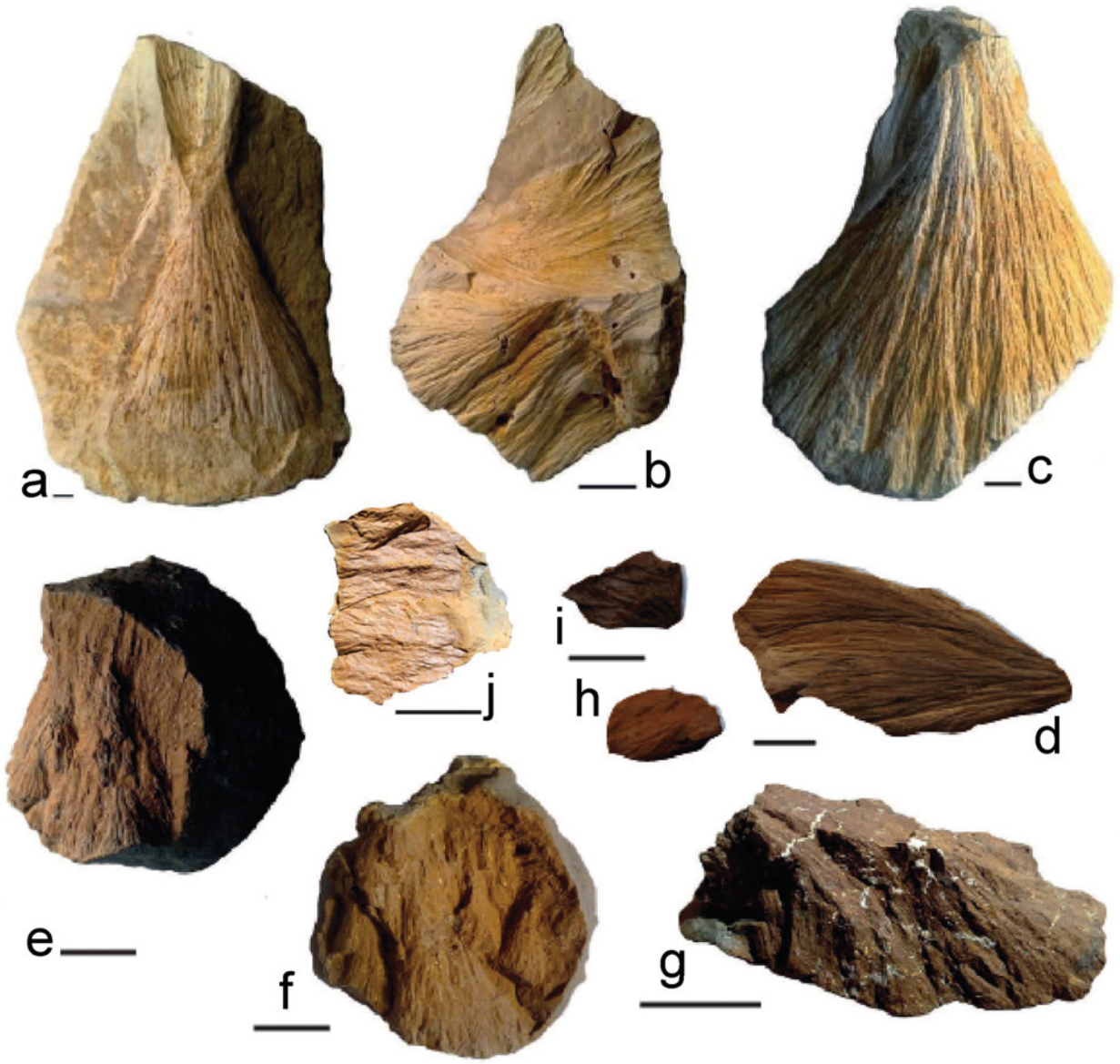

Figure 3. (Colour online) Typical shatter cones in Upper Jurassic (Kimmeridgian–Tithonian) limestones at Steinheim (a–d) and in concretions of the Middle Jurassic Opalinus Claystone (e–j): (a) Hourglass-like shatter cone with positive (convex, above) and negative (concave, below) individual cones running in opposite directions; (b) nested aggregate of shatter cones building up a 'horsetail'-structured limestone specimen (below) and a negative individual shatter cone (above); (c) well-developed larger individual cone; (d) well-developed individual cone investigated in this study (SC-L1; Table 2) coated with carbon for SEM–EDS analysis; (e–j): shatter cones in Middle Jurassic Opalinus Claystone nodules: (e, f) horsetail structure with a set of nested positive (convex) individual shatter cones running in one main direction across the whole nodule; (g) well-defined shatter cone in claystone showing white, opalescent remnants of fossil shells; (h) small Opalinus Claystone shatter cone individual investigated in this study (SC-C2; Table 1), not carbon coated; (i) small Opalinus Claystone shatter cone individual investigated in this study (SC-C3; Table 1), carbon coated; (j) Opalinus Claystone shatter cone covered by a bright, shiny coating; sample courtesy: Peter Seidel, Steinheim am Albuch. Scale bars are 1 cm. Shatter cone photographs compiled from Schmieder & Buchner (2013) and from shatter cones of the impactite collection at the Institut für Mineralogie und Kristallchemie, Universität Stuttgart, curated by the authors.

2. The Steinheim Basin: geologic setting

The ∼ 3.8 km diameter Steinheim Basin, centred at 48° 41′ N, 10° 04′ E, about 42 km SW of the centre of the Ries crater, is a complex impact crater with a prominent central uplift formed in a sequence of Triassic and Jurassic sedimentary rocks that build up the karstified limestone plateau of the eastern Swabian Alb (Baden-Württemberg, SW Germany; e.g. Reiff, 1976, 1977; Hüttner & Schmidt-Kaler, 1999; Heizmann & Reiff, 2002; Ivanov & Stöffler, 2005; Buchner & Schmieder, 2015; Figs 1, 2). A minor portion of the target rocks probably involved Palaeogene (bog iron ore-type 'Bohnerz Formation') to Neogene (sandy deposits of the Miocene 'Upper Freshwater Molasse') sediments. Owing to the protective post-impact sedimentary cover, among which are fossil-rich Miocene crater lake sediments, the Steinheim Basin is one of the best-preserved complex impact craters

https://doi.org/10.1017/S0016756816001357 Published online by Cambridge University Press

on Earth (e.g. Heizmann & Reiff, 2002). The morphological crater rim exhibits inclined and brecciated blocks and clods of Upper Jurassic (Kimmeridgian to Tithonian) marine limestones (Heizmann & Reiff, 2002; Reiff, 2004) locally rich in chert nodules. A mainly carbonatic lithic impact breccia (earlier referred to as '*Primäre Beckenbrekzie*' by Groschopf & Reiff, 1966, 1969) is known from numerous drillings into the Steinheim Basin (Reiff, 2004) and contains variable amounts of lithic clasts of Middle to Upper Jurassic limestones, marls, mudstones and sandstones.

Although there is still no striking evidence for higher levels of shock metamorphism in mineral grains, the Steinheim Basin is well known for its brecciated rocks and shatter cones (mainly in micritic limestones) of exemplary shape and quality (e.g. Dietz, 1959, 1960; Dietz & Butler, 1964; von Engelhardt *et al*. 1967; Heizmann & Reiff, 2002; Fig. 3). Melt lithologies from the Steinheim Basin were reported by Buchner & Schmieder (2010; carbonate-dominated suevitic impact breccia) and Anders *et al*. (2013; carbonatic impact melt rock). Isotopic dating has, so far, not yielded a geologically meaningful age (e.g. Buchner *et al*. 2013). The Steinheim impact structure is thought to have formed simultaneously with the ~24 km Nördlinger Ries crater by the impact of a binary asteroid at 14.83 ± 0.15 Ma (Di Vincenzo & Skála, 2009; see also Buchner *et al*. 2010, 2013), which is roughly consistent with the Miocene post-impact crater lake biostratigraphy at both impact craters (Reiff, 1988, 2004; Stöffler, Artemieva & Pierazzo, 2002; Buchner *et al*. 2010, 2013; and see Schmieder *et al*. 2014 for discussion). Findings of Fe–Ni–Co sulfides and Fe–Ni-droplets associated with the Steinheim melt lithologies were interpreted to suggest an iron meteoritic impactor (Schmieder & Buchner, 2009, 2010*b*; Buchner & Schmieder, 2010; Anders *et al*. 2013).

Deformation caused by the Steinheim impact mainly affected Jurassic sedimentary rocks. Crater-filling impact ejecta deposits contain abundant clasts of Upper to Middle Jurassic rocks, whereas fracturing, faulting and structural uplift (~ 350 m at the centre of the Steinheim Basin) reach down to the Upper Triassic (the continental 'Stubensandstein' Keuper sandstones; e.g. Heizmann & Reiff, 2002; Reiff, 2004; Buchner & Schmieder, 2013*b*, their fig. 4). Middle Jurassic (Upper Aalenian) iron-rich and locally shatter-coned marine 'Eisensandstein' sandstones (e.g. Schmieder & Buchner, 2013, their fig. 4) build up the flanks of the central uplift. At the centre of the Steinheim central uplift (locally known as the '*Steinhirt*' and '*Klosterberg*' hills south of the village of Steinheim am Albuch; Fig. 2), the Middle Jurassic (Lower Aalenian) marine, black shale-type 'Opalinuston' Claystone formation (attaining up to >100 m in thickness in Eastern Württemberg; Geyer & Gwinner, 1991; Reiff, 2004) crops out and locally causes surficial effects of waterlogging (visible in the field at the '*Lettenhülbe*' pond situated on top of the central uplift). The strongly squeezed Opalinus Claystone strata are in an almost upright position in the upper parts of the central uplift and still show a ~ 60° basin-ward inclination at a depth of 200 m (Reiff, 1976; Heizmann & Reiff, 2002).

3. Samples, sample localities and analytical techniques

Shatter cones in the Middle Jurassic Opalinus Claystone were sampled on top of the Steinheim central uplift (Steinhirt; 48° 41′ 07″ N, 10° 03′ 50″ E) during water catchment works in April 2010; Figs 2, 3; see also Schmieder & Buchner, 2013, their fig. 5, for images of the temporary exposure). Shatter cones of the 'classical' Steinheim-type in Upper Jurassic limestones (Fig. 3) were collected on fields halfway between the northern flank of the '*Burgstall*' (48° 40′ 30″ N, 10° 04′ 19″ E) and '*Knill*' (48° 40′ 34″ N, 10° 04′ 38″ E) hills close to the southeastern rim of the Steinheim Basin. In this study, we investigated 11 shatter cone specimens (between ~ 1 and ~ 3 cm in size) taken from six different Opalinuston Claystone nodules. The occurrences of rare metals were detected on five of these shatter cone individuals; these samples are denominated 'Shatter Cone Claystone 1–5' (SC-C1 to SC-C5) in the following. Furthermore, we analysed four larger (between ~ 4 and ~ 6 cm in size) individual shatter cones in Upper Jurassic limestone, referred to as 'Shatter Cone Limestone 1–4' (SC-L1 to SC-L4) in the text.

Geochemical analyses of the coatings on shatter cone surfaces were carried out by scanning electron microscopy and energy-dispersive X-ray spectroscopy (SEM–EDS) using a CamScan SC44 scanning electron microscope coupled to an EDAX PV 9723/10 system (Institut für Mineralogie und Kristallchemie, Universität Stuttgart), at a beam current of 70 nA and acceleration voltages of 15 and 20 kV. The system is equipped with a conventional Be window Si(Li) detector 13 µm in thickness. Standard counting times were 300 seconds. All analyses are normalized to 100 wt % and oxygen were calculated by stoichiometry. ZAF matrix correction software was used to calculate element concentrations. Imaging was done in secondary electron (SE) and backscattered electron (BSE) mode. To avoid contamination of the shatter cone samples with Au, C or other elements from the sputter apparatus, a certain number of SEM–EDS analyses were carried out on uncoated specimens that were also analysed under high vacuum conditions. Microspec™ olivine, apatite and cryolite (analysed by the Oxford Instruments™ Microanalysis Group) were used as compound standards for EDS analyses. Further standards used (analysed by the Oxford Instruments™ Microanalysis Group) are barite for Ba; pyrite (villamaninite) for S, Ni, Co and Cu; pure platinum for Pt; and pure gold for Au. The accuracy of the analyses varied depending on the roughness of the sample surfaces, but all analyses shown in this study were above the detection limits indicated in the tables.

https://doi.org/10.1017/S0016756816001357 Published online by Cambridge University Press

The very high content in Fe (around 90 wt %; see Table 1, e.g. Fig. 3f) of the coatings of some of the Opalinus Claystone shatter cones and the resultant high conductivity of the surfaces of these shatter cones allows imaging and EDS analyses on uncoated specimens without disturbing charging processes. The SEM–EDS (EDAX PV 9723/10) system of the Stuttgart SEM laboratory is able to detect C and O qualitatively, but not quantitatively. However, the system allows the user to determine with some certainty whether the phases analysed are oxides, carbonates, sulfates or sulfides. Oxygen was analysed qualitatively to discriminate between metal and oxide phases in our samples.

Because of the interferences between Mn, Fe, Co and Ni emission lines, the evaluation of EDS spectra is sometimes difficult. This holds particularly true for the measurement of Co in the presence of Fe and Ni, because the Fe-Kβ line overlaps with the Co-Kα line, and the Co-Kβ line is covered by the Ni-Kα line. We assumed the qualitative presence of Co, if the following two criteria were fulfilled: (1) the Co-Kα line is situated somewhat to the left of the Fe-Kβ line and the Co-Kβ line somewhat to the right of the Ni-Kα line, leading to an asymmetric appearance of the Fe-Kβ and Ni-Kα peaks (when Co-Kα and Co-Kβ lines are covered); and (2) in the case where the Fe-Kβ overlaps with the Co-Kα line, the resultant apparent Fe-Kβ peak will be disproportionally high compared to the Fe-Kα peak.

For verification of the SEM–EDS results, metallic particles were scraped off the shatter cone surfaces using a scalpel and embedded in synthetic resin, from which polished thin-sections were produced and analysed by electron probe microanalysis (EPMA; SC-C6 and SC-L5). In order to prevent contamination of our samples with rare metals, we analysed all tools (hammer, scalpel and tweezers) used in the preparation process. The steel composition of these tools exclusively comprised Fe, Mn, C and Cr. Electron probe microanalysis and wavelength-dispersive spectrometric (WDS) scans were carried out with a CAMECA™ SX 100 electron microprobe equipped with five WDS spectrometers (Institut für Mineralogie und Kristallchemie, Universität Stuttgart). The electron beam diameter was 5 μm at a current of 5/10 nA (35 nA for WDS scans) and an acceleration voltage of 20 kV; standard counting times were 180 seconds. The system is able to detect O qualitatively and quantitatively. The CAMECA™ SX 100 is equipped with PeakSight EPMA automation and analysis software. EPMA precision for standardless analysis is 2–3 % for major elements, but can exceed 10 % for elements with values <2 wt % in individual cases. Estimated accuracy (total EPMA error) amounts to ~ 5 % for major elements. Quantitatively, all elements analysed by SEM–EDS (listed in Tables 1 and 2) were detected well above the EPMA detection limits and background, and all analyses were carried out on individually and randomly composed coatings that do not reflect primary mineral composition. WDS scans, not done quantitatively, were carried out to control EPMA results, particularly the crucial sector of the EDS spectra of Mn, Fe, Ni and Co peak interference.

4. Petrography and geochemistry

4.a. Coatings on Middle Jurassic Opalinus Claystone shatter cones (SC-C1 to SC-C6)

The Opalinus Claystone in southern Germany is modally dominated by clay minerals (~65 % illite–smectite mixed layers), quartz (~19 % sand and silt), calcite (~13 %) and some accessories such as siderite (Fe-carbonate), pyrite, feldspar and organic carbon (Kobler, 1972; Etzold, 1994; Heitzmann & Bossart, 2001). Concretionary claystone nodules and competent carbonatic layers characterized by diagenetic cone-in-cone structures (e.g. Selles-Martinez, 1994; Schmieder & Buchner, 2010*a*) are commonly observed in the Opalinus Claystone. The nodules are of marly, sideritic and rarely of phosphatic composition, with variable contents of Ca- and Fe-carbonate (Andalib, 1970; Kobler, 1972; Brodbeck, 1995). Shatter cones in the Opalinus Claystone have only been found in these rather competent nodules.

Thin coatings on freshly exposed shatter cone surfaces in the Opalinus Clay are visible on the mesoscopic scale as a clear to reddish-yellow, silky 'patina' (Fig. 4). In SEM–EDS analyses, the surfaces of all 11 shatter cone individuals revealed coatings (Figs 5, 6) rich in Fe, Ca, P, Si, K and Al (quantified as the respective oxides Fe_2O_3, CaO, P_2O_5, SiO_2, K_2O and Al_2O_3, for shatter cones SC-C1 through SC-C5, see Table 1) in highly variable proportions that geochemically resemble the cementing material (marl, siderite, phosphate) of the Opalinus Claystone nodules. Furthermore, Mg, Mn, S, Ti, Ni, Co, Cu and Au concentrations are locally in the per cent range. In some of the coatings (in particular, that of sample SC-C4), Ba, S and Ca concentrations are locally elevated owing to the occurrence of secondary barite and/or Ca-sulfate (gypsum/anhydrite) aggregates (see Table 1).

Five (SC-C1 to SC-C5) of the 11 studied shatter cone individuals revealed additional elements in the per cent range (see Table 1). EDS-resolvable amounts of Cu and Pt were detected on the surface of samples SC-C1 (Table 1) and SC-C3 (Table 1), respectively. Nickel, cobalt and gold are abundant in nearly every measurement on the five shatter cone individuals SC-C1 through SC-C5 (Table 1). Notably, gold forms very small disseminated micro-grains (SC-C1 and SC-C4; Table 1) or nests of small aggregates of native Au (SC-C5; Table 1). The gold aggregates are commonly coated by a very thin Ca- and Fe-rich layer (quantified as CaO and Fe_2O_3). In only one case, a homogeneous particle rich in Fe, Ni and Co (quantified as oxides) was found on the surface of an Opalinus Claystone shatter cone. In contrast to the geochemically variable coating, SEM–EDS analyses on the entire grain surface yielded very similar analytical results within relatively

https://doi.org/10.1017/S0016756816001357 Published online by Cambridge University Press

Table 1. SEM–EDS analyses (SC-C1 to SC-C5) (20 kV) of coatings on the surfaces of five shatter cone individuals in Middle Jurassic Opalinus Claystone concretions

Sample	SC-C1 (single)		SC-C1 (range)	SC-C2 (single)		SC-C2 (range)	SC-C3 (single)		SC-C3 (range)	SC-C4 (single)		SC-C4 (range)	SC-C5 (single)		SC-C5 (range)	Sample	SC-C6 #1		SC-C6 #2		SC-C6 #3	
Oxides (SEM-EDS) (wt %)	Coating on Opalinus Clay shatter cone		Coating on Opalinus Clay shatter cone; range of ten analyses	Coating on Opalinus Clay shatter cone		Coating on Opalinus Clay shatter cone; range of ten analyses	Coating on Opalinus Clay shatter cone		Coating on Opalinus Clay shatter cone; range of ten analyses	Coating on Opalinus Clay shatter cone		Coating on Opalinus Clay shatter cone; range of ten analyses	Coating on Opalinus Clay shatter cone		Coating on Opalinus Clay shatter cone, range of six analyses	Elements EPMA (wt %)	Metallic particles scraped from three claystone shatter cone surfaces; thin-sections					
Int. error		±1σ			±1σ			±1σ			±1σ			±1σ				±1σ		±1σ		±1σ
SiO_2	1.86	0.2	1.80–1.99	0.85	0.2	0.25–1.25	6.12	0.3	2.28–9.72	4.07	0.3	3.82–4.01	0.20	0.1	0.18–0.26	Si	2.13	0.2	1.76	0.2	1.10	0.2
Al_2O_3	0.66	0.2	0.65–0.77	0.50	0.2	0.58–0.68	5.54	0.3	0.96–10.27	n.d.		0.00–0.05	0.88	0.2	0.81–1.18	Al	4.08	0.3	5.38	0.3	4.72	0.3
Fe_2O_3	73.01	0.4	73.01–82.16	94.28	0.5	94.28–96.67	69.71	0.5	47.12–70.94	11.01	0.4	8.36–11.01	87.70	0.5	86.85–89.42	Fe	57.01	0.5	55.96	0.5	58.05	0.5
CaO	8.70	0.3	8.61–9.00	0.54	0.2	0.54–0.55	11.12	0.4	5.69–18.81	1.55	0.2	1.42–1.62	0.23	0.1	0.22–1.38	Ca	7.55	0.4	5.28	0.3	1.35	0.3
K_2O	0.23	0.1	0.23–0.33	n.d.		0.00–0.13	3.36	0.3	0.66–9.65	n.d.		n.d.	n.d.		n.d.	K	n.d.		n.d.		n.d.	
MgO	0.29	0.1	0.28–0.31	n.d.		0.00–0.11	n.d.		0.00–0.51	n.d.		0.00–0.10	n.d.		0.00–0.12	Mg	n.d.		n.d.		0.89	0.2
SO_2	0.87	0.2	0.81–0.88	n.d.		0.00–0.03	0.20	0.1	0.20–0.23	17.4	0.4	17.30–17.55	n.d.		n.d.	S	n.d.		n.d.		n.d.	
MnO	1.57	0.2	0.00–1.66	1.11	0.2	1.07–1.43	1.13	0.2	0.65–1.46	0.57	0.2	0.49–0.69	2.22	0.2	1.48–2.91	Mn	2.39	0.3	1.99	0.2	1.15	0.2
Na_2O	n.d.		0.00–1.53	n.d.		n.d.	n.d.		n.d.	n.d.		n.d.	n.d.		n.d.	Na	n.d.		n.d.		n.d.	
P_2O_5	0.50	0.2	0.37–0.57	n.d.		0.00–0.07	n.d.		0.00–3.93	0.66	0.2	0.62–0.90	n.d.		n.d.	P	0.88	0.2	1.14	0.2	2.21	0.2
TiO_2	n.d.		n.d.	n.d.		0.00–0.10	1.02	0.2	0.15–2.57	n.d.		n.d.	n.d.		n.d.	Ti	n.d.		n.d.		n.d.	
																O	21.26	0.3	20.69	0.3	22.06	0.3
NiO	0.80	0.2	0.21–0.84	0.60	0.2	0.28–0.64	1.13	0.3	0.34–1.31	0.60	0.2	0.40–0.61	0.58	0.2	0.58–0.60	Ni	2.30	0.4	4.51	0.4	2.18	0.3
CoO	0.54	0.2	0.00–0.66	2.12	0.3	2.01–2.22	0.67	0.2	0.06–1.38	0.45	0.2	0.41–0.59	8.19	0.4	7.98–9.55	Co	1.22	0.3	1.10	0.3	5.09	0.3
CuO	10.09	0.3	9.65–10.12	n.d.		n.d.	n.d.		n.d.	n.d.		0.00–0.00	n.d.		n.d.	Cu	0.91	0.2	2.30	0.2	1.06	0.2
Au	0.88	0.2	0.86–1.01	n.d.		0.00–0.10	n.d.		0.00–0.33	1.17	0.2	1.71–1.89	n.d.		0.00–94.52	Au	n.d.		n.d.		n.d.	
PtO	n.d.		n.d.	n.d.		n.d.	n.d.		0.00–1.45	n.d.		n.d.	n.d.		n.d.	Pt	n.d.		n.d.		n.d.	
BaO	n.d		0.51–1.55	n.d.		n.d.	n.d.		n.d.	62.52	0.5	61.84–65.22	n.d.		n.d.	Ba	n.d.		n.d.		n.d.	
Total	100.00			100.00			100.00			100.00			100.00			Total	99.73		100.11		99.86	

Element values in oxide wt %; normalized to 100 %; EPM analyses on sample SC-C6 were carried out on polished thin-sections of particles scraped from three Opalinus Claystone shatter cone surfaces; the presence of Mn, Fe, Ni and Co in electron probe microanalyses was qualitatively confirmed by WDS scans.

Table 2. SEM–EDS analyses (20 kV) of coatings on the surfaces of three individuals of Upper Jurassic limestone shatter cones (SC-L1 to SC-L3)

Sample	SC-L1 (single)	SC-L1 (range)	SC-L2 (single)	SC-L2 (range)	SC-L3 (single)	SC-L3 (range)	Sample	SC-L5 #1	SC-L5 #2	SC-L5 #3	SC-L5 #4	SC-L5 #5
Oxides (SEM–EDX) (wt %)	Coating on limestone shatter cone surface	Coating on limestone shatter cone; range of 15 analyses	Coating on limestone shatter cone surface	Coating on limestone shatter cone; range of 14 analyses	Coating on limestone shatter cone surface	Coating on limestone shatter cone; range of 15 analyses	Elements (EPMA) (wt %)	Metallic particles scraped from three limestone shatter cone surfaces; thin-sections; for numbers of samples see Fig. 7a.				
Int. error	± 1σ		± 1σ		± 1σ			± 1σ	± 1σ	± 1σ	± 1σ	± 1σ
SiO_2	3.11 0.3	3.18–3.26	1.24 0.2	0.22–1.90	1.47 0.2	0.38–2.55	Si	0.53 0.06	0.46 0.04	3.25 0.05	0.50 0.05	0.51 0.07
Al_2O_3	2.02 0.2	1.99–2.14	1.34 0.2	0.47–1.36	1.23 0.2	1.11–1.39	Al	6.67 0.07	6.51 0.10	1.84 0.08	6.48 0.08	6.61 0.05
Fe_2O_3	10.89 0.3	6.90–11.01	3.29 0.3	3.10–3.34	60.69 0.4	1.24–89.87	Fe	2.21 0.18	1.93 0.16	11.26 0.21	2.24 0.16	2.26 0.10
CaO	61.12 0.4	58.76–61.30	53.92 0.4	40.62–57.78	6.33 0.3	6.32–59.34	Ca	10.74 0.09	14.17 0.10	17.47 0.18	10.51 0.07	8.61 0.08
K_2O	0.67 0.2	0.65–0.70	0.99 0.2	0.96–1.21	0.32 0.1	0.26–1.11	K	0.08 0.02	n.d	0.56 0.06	0.10 0.01	0.08 0.02
MgO	n.d.	0.00–0.39	n.d.	0.00–0.22	n.d.	0.00–0.27	Mg	0.73 0.06	0.82 0.05	n.d.	0.65 0.06	0.86 0.07
SO_2	n.d.	0.00–0.27	0.20 0.1	0.19–0.20	7.49 0.2	0.00–14.54	S	n.d.	n.d.	0.36 0.04	n.d.	n.d.
MnO	18.74 0.4	16.34–18.82	35.12 0.4	32.07–46.34	n.d.	0.00–0.21	Mn	43.15 0.26	42.11 0.17	37.65 0.26	45.82 0.25	46.42 0.18
P_2O_5	0.55 0.2	0.40–0.61	n.d.	0.21–0.37	n.d.	0.00–4.78	P	n.d.	n.d.	n.d.	n.d.	n.d.
							O	26.77 0.11	26.73 0.13	21.23 0.16	26.25 0.08	26.70 0.09
NiO	1.65 0.3	1.61–1.66	2.89 0.3	2.47–3.07	5.51 0.3	0.23–6.99	Ni	7.31 0.19	5.19 0.18	4.02 0.17	5.11 0.17	5.56 0.16
CoO	0.59 0.2	0.50–0.65	0.55 0.2	0.54–0.58	2.22 0.3	0.35–3.28	Co	1.97 0.16	1.84 0.15	2.34 0.15	2.68 0.15	2.21 0.15
CuO	n.d.	n.d.	n.d.	n.d.	n.d.	0.00–31.07	Cu	n.d.	n.d.	n.d.	n.d.	n.d.
Au	0.66 0.2	0.58–0.75	0.46 0.2	0.20–0.57	n.d.	0.00–88.98	Au	n.d.	n.d.	n.d.	n.d.	n.d.
PtO	n.d.	n.d.	n.d.	n.d.	n.d.	n.d.	Pt	n.d.	n.d.	n.d.	n.d.	n.d.
BaO	n.d.	n.d.	n.d.	n.d.	14.74 0.4	0.00–45.96	Ba	n.d.	n.d.	n.d.	n.d.	n.d.
ZnO	n.d.	n.d.	n.d.	n.d.	n.d.	0.00–41.57*	Zn	n.d.	n.d.	n.d.	n.d.	n.d.
Total	100.00		100.00		100.00		Total	100.16	99.76	99.98	100.34	99.82

Element values in oxide wt %; analyses normalized to 100 %; EPM analyses on sample SC-L5 were carried out on polished thin-sections of particles scraped from Upper Jurassic limestone shatter cone surfaces; the presence of Mn, Fe, Ni and Co in electron probe microanalyses was qualitatively confirmed by WDS scans.

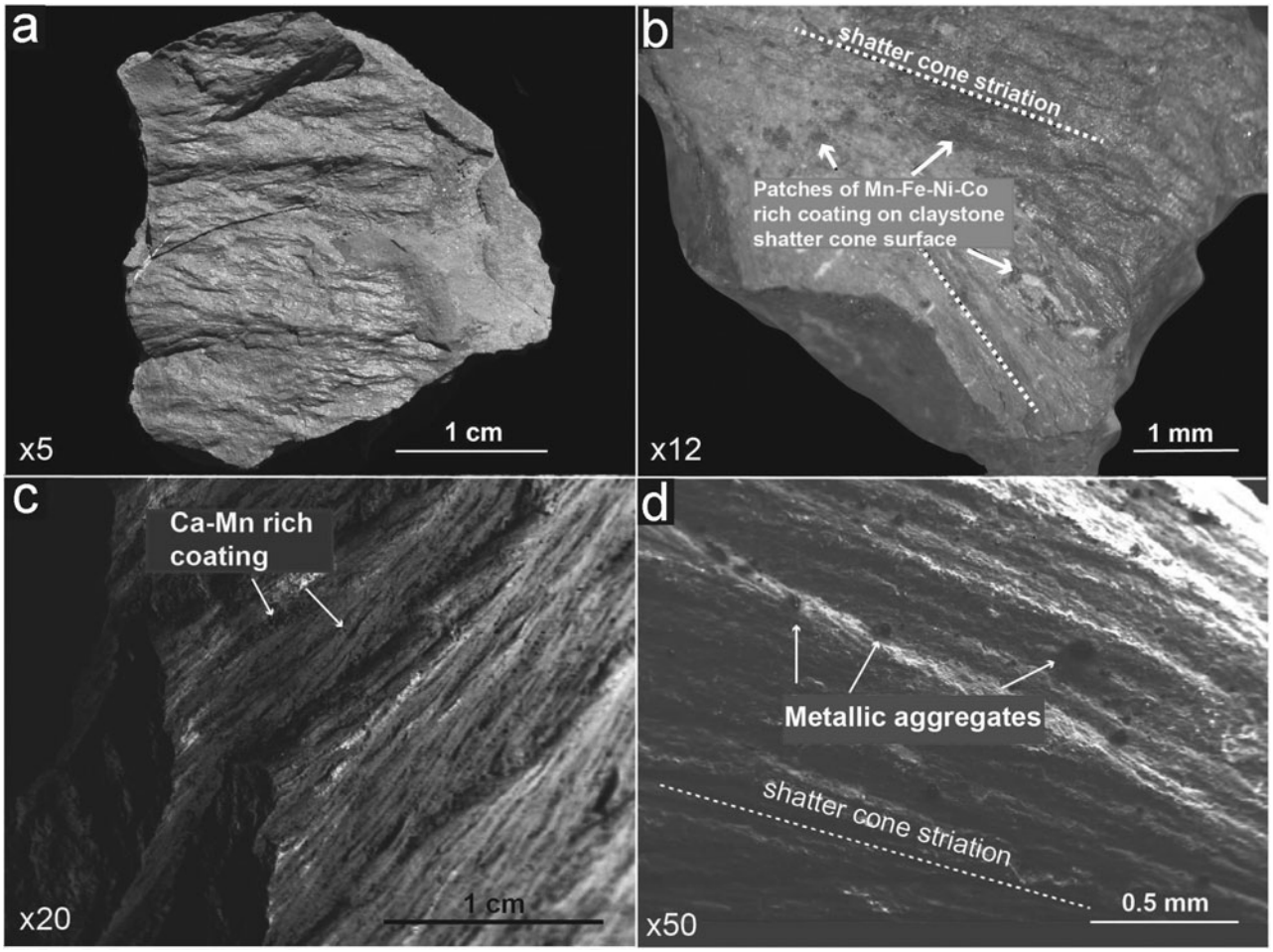

Figure 4. Coatings on Middle Jurassic claystone shatter cones (a, b) and on Upper Jurassic limestone shatter cones (c, d). In some rare cases, thin coatings can cover the entire shatter cone surface (a); they mostly occur in patches (b) or are aligned along the shatter cone striations (c), or as single aggregates randomly distributed on shatter cone surfaces (d).

narrow limits (SC-C5; Table 1). Samples of the coatings scraped off three claystone shatter cone specimens also contained individual aggregates rich in Fe, Ni, Co and Cu (SC-C6; Table 1).

4.b. Coatings on Upper Jurassic limestone shatter cones

Limestone shatter cones from the Steinheim Basin sometimes exhibit a characteristic brownish or greenish to grey staining (including micro-dendrites of iron and manganese oxides and oxyhydrates; Fig. 4) of the striated surface, on a hand specimen scale. The Upper Jurassic limestones of the Steinheim area are mainly composed of calcite (~80–86 wt % CaO) and dolomite (~0.8–1.2 wt % MgO), some sulfate (~1.3–1.7 wt % SO_3), detrital quartz grains and phyllosilicates (~5.1–6.2 wt % SiO_2, ~1.7–2.9 % Al_2O_3, ~1.0–1.7 wt % K_2O, ~0.9–2.4 wt % Fe_2O_3), in variable proportions. The surfaces of two SEM-investigated limestone shatter cones (SC-L1 and SC-L2) show a thin layer rich in CaO and MnO (in the form of calcite and manganese oxides/hydroxides). Furthermore, K-rich phyllosilicates (probably illite as a common mineral in weathered Jurassic limestones, e.g. Kobler, 1972) occur in the limestone shatter cone coatings (see Table 2). Between the shatter cone surfaces and the Ca–Mn-rich coating, some optically darker (light in BSE images) patches rich in Fe, Ni and Co (again, quantified as oxides) are dispersed across the shatter cone surface (SC-L1 and SC-L2; Table 2). Larger aggregates of native gold are not visible in the SEM; however, measured values for Au concentrations reach up to ~0.75 wt % in these patches, obviously caused by finely dispersed Au tinsel. It was technically not possible to analyse the Fe-, Ni-, Co- and Au-rich patches directly, as all these patches were covered by the Mn- and Ca-rich coating (Table 1). Besides Fe, Ni, Co, Cu and Au, no further elements were detected by SEM–EDS measurements in the per cent range. Coatings scraped off shatter cone surfaces showed oxide aggregates enriched in Ca and Mn, as well as in Fe, Ni and Co (SC-L5; Table 2; Fig. 7).

The coating on the surface of an Upper Jurassic limestones shatter cone sample (SC-L3) is dominated by CaO, Fe_2O_3 and some phyllosilicates, but essentially free of Mn (see Table 2). The shatter cone surface is covered by a macroscopically visible greenish to grey coating, occurring parallel to the shatter cone striation. These coatings exhibit countless aggregates and very fine grains and larger aggregates of native Au

https://doi.org/10.1017/S0016756816001357 Published online by Cambridge University Press

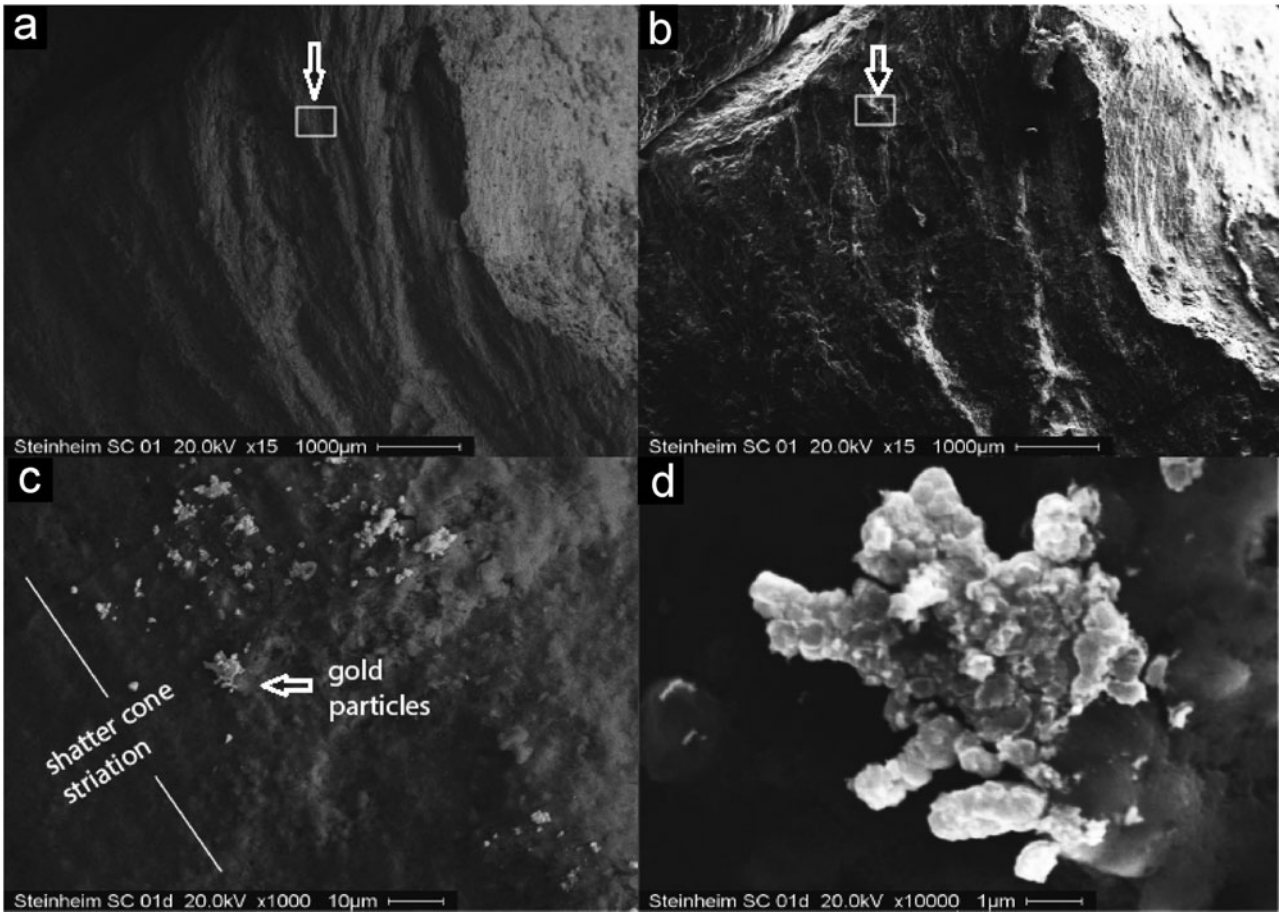

Figure 5. Opalinus Claystone shatter cone (SC-C5), coated by presumed hydrothermal mineralization including aggregates of native gold. (a) Shatter cone surface showing well-developed horse-tail structures (secondary electron image). (b) Shatter cone surface, same as (a) (backscattered electron image); frame shows area with gold aggregates shown in (c) and (d). (c) Small gold aggregates imbedded in shatter cone coating; arrow shows gold aggregate depicted in (d). (d) Single gold aggregate grown on Fe-rich substrate; gold aggregate is covered by a thin Ca- and Fe-rich coating.

(Figs 8, 9; concentrations given as oxide wt %), as well as non-metallic areas with elevated concentrations of Fe, Ni, Co, Cu, Pt and Au in highly variable proportions, embedded in the Ca–Fe-rich coating, which on this shatter cone specimen is nearly free of Mn. Furthermore, a single grain rich in Cu and Zn and multiple barite grains were encountered.

On the surface of limestone shatter cone sample SC-L4 (Fig. 10; Table 3), we detected a single botryoidal flake ~400 µm in maximum length that consists of a 'lighter' and a 'darker' portion in BSE image mode. Qualitative EDS analysis of oxygen revealed that both phases are, at least at the surface of the aggregate, oxides. Six SEM–EDS measurements on the lighter portion of the flake revealed high values in Fe (~65.2–88.0 wt % Fe_2O_3), Ni (~7.5–9.1 wt % NiO) and Co (~0.9–2.1 wt % CoO), and a minor content in SiO_2, MgO and CaO (Table 3). Some measurements yielded additional significant contents of Cu (≤18.9 wt % CuO), Pt (≤2.1 wt % PtO), Ge (~0.8–2.3 wt % GeO_2) and Ga (~0.7–0.8 wt % Ga_2O_3; Table 3). Six individual measurements resulted in a more siliceous composition of the darker portion of the flake, with high concentrations of silica (~24.4–46.9 wt % SiO_2), Al_2O_3 (~4.3–19.0 wt %), CaO (~6.7–23.1 wt %) and MgO (~2.6–6.3 wt %), versus lower, but still considerable, concentrations of Fe, Ni and Co (given as oxides), compared to the brighter portion of the flake. The darker portion of the flake, however, also revealed notable Cu, Pt, Ga and Ge concentrations in the oxide phase (see Table 3).

5. Discussion

5.a. Origin of the Steinheim shatter cone coatings

5.a.1. Contamination from the Mesozoic sedimentary target rock?

In the Steinheim Basin area, several of the Mesozoic–Cenozoic sedimentary units can be considered as potential sources for rare metals detected in the coatings on shatter cone surfaces. Calcium carbonate, manganese oxides and minor phyllosilicates, found associated with the surface coating of two Upper Jurassic limestone shatter cones (SC-L1 and SC-L2), are omnipresent in fluids in sedimentary rocks of the Swabian Alb, and commonly form thin coatings on faults, bedding planes and in cavities in the bedrock. The fossiliferous black shale deposits of the Lower and Middle Jurassic (including the Sinemurian

https://doi.org/10.1017/S0016756816001357 Published online by Cambridge University Press

Table 3. Twelve individual SEM–EDS measurements (1 to 6 on the light, metal-rich portion and 7 to 12 on the dark more siliceous portion) on a Fe-, Ni- and Co-rich oxide flake on the surface of an Upper Jurassic limestone shatter cone individual (SC-L4; compare to Fig. 7)

	SiO_2	±1σ	Al_2O_3	±1σ	CaO	±1σ	MgO	±1σ	Fe_2O_3	±1σ	NiO	±1σ	CoO	±1σ	CuO	±1σ	PtO	±1σ	GeO_2	±1σ	Ga_2O_3	±1σ
SC-L4; bright portion of flake																						
1	1.3	0.2	n.d.		n.d.		n.d.		88.0	0.3	9.1	0.3	1.6	0.2	n.d.		n.d.		n.d		n.d.	
2	1.7	0.2	n.n		n.d.		n.d.		87.9	0.3	9.1	0.3	1.3	0.2	n.d		n.d.		n.d.		n.d.	
3	2.1	0.2	n.d.		1.1	0.2	0.8	0.2	85.4	0.3	8.8	0.3	1.0	0.3	n.d.		n.d.		0.8	0.2	n.d.	
4	1.7	0.2	n.d.		0.8	0.2	0.8	0.2	84.8	0.3	9.1	0.2	0.9	0.2	n.d.		n.d.		1.2	0.2	0.7	0.2
5	1.2	0.2	n.n		0.9	0.2	n.d.		85.6	0.4	9.0	0.3	1.4	0.2	n.d.		n.d.		1.2	0.2	0.7	0.2
6	1.2	0.2	n.d.		n.d		n.d.		65.2	0.3	7.5	0.2	2.1	0.2	18.9	0.3	2.1	0.2	2.3	0.2	0.7	0.2
SC-L4; dark portion of flake																						
7	42.1	0.3	18.3	0.2	11.8	0.3	2.6	0.2	19.00	0.3	5.1	0.4	1.1	0.3	n.d.		n.d.		n.d.		n.d.	
8	46.9	0.3	11.6	0.3	15.8	0.4	4.4	0.3	15.1	0.4	5.6	0.3	0.6	0.2	n.d.		n.d.		n.d.		n.d.	
9	38.0	0.3	4.3	0.2	23.1	0.3	n.d.		24.3	0.3	8.3	0.3	2.0	0.3	n.d.		n.d		n.d.		n.d.	
10	46.1	0.3	9.5	0.3	6.7	0.2	3.4	0.2	26.6	0.4	5.9	0.3	1.8	0.3	n.d.		n.d.		n.d.		n.d.	
11	24.4	0.3	9.9	0.2	8.5	0.4	2.9	0.3	20.7	0.3	2.7	0.3	1.2	0.3	21.8	0.4	4.4	0.3	1.9	0.3	1.6	0.2
12	25.3	0.4	19.0	0.3	13.5	0.3	6.3	0.2	19.2	0.2	2.3	0.3	1.1	0.3	9.9	0.3	n.d.		1.6	0.3	1.8	0.3

Elements in oxide wt %; normalized to 100 %.

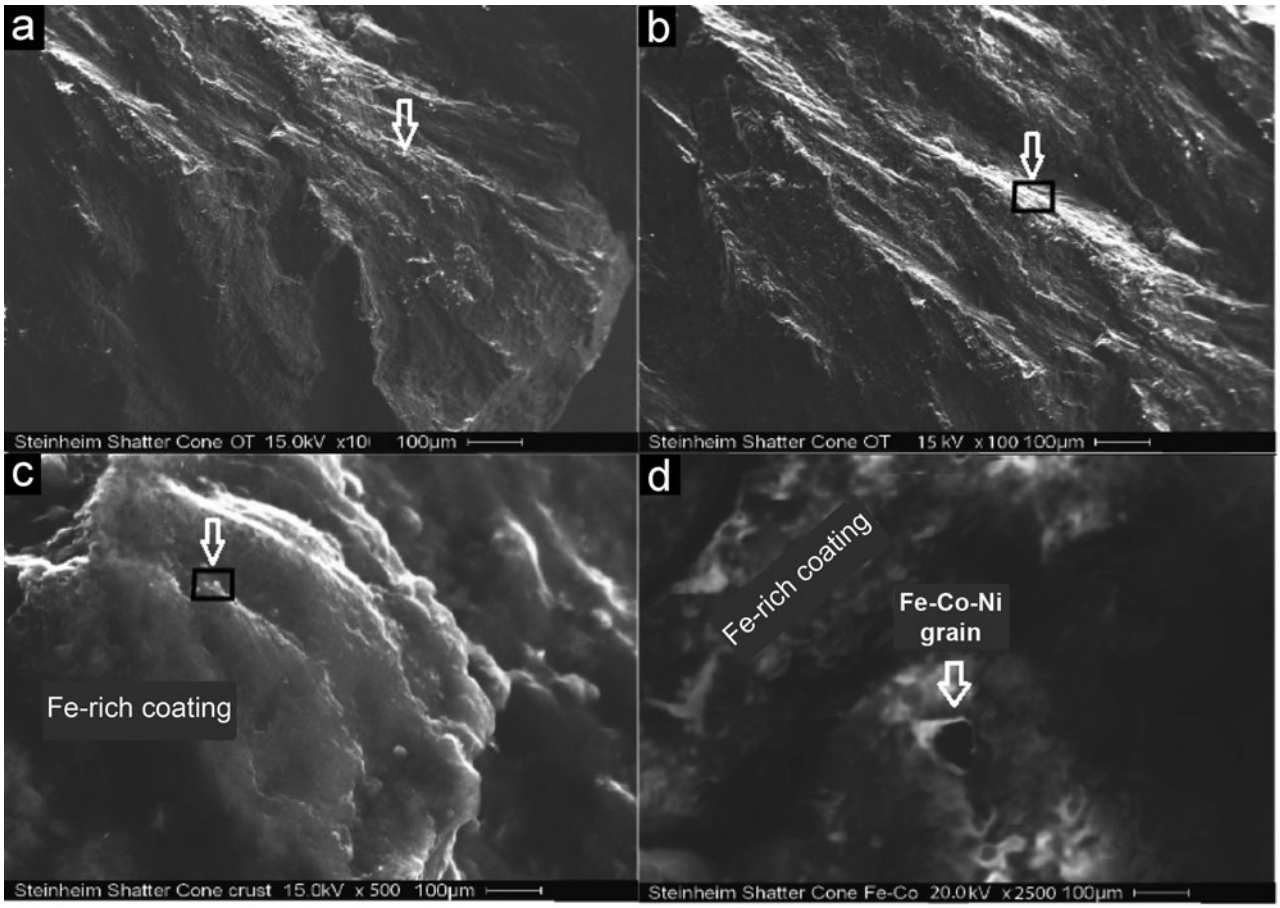

Figure 6. Opalinus Claystone shatter cone (sample SC-C5), covered by Ca- and Fe-rich coating and a Fe–Co–Ni-rich particle. (a) Shatter cone surface showing well-developed horse-tail structures (secondary electron image); arrow shows sector depicted in (b). (b) Shatter cone surface showing well-developed horse tail structures (secondary electron image); arrow shows sector depicted in (c). (c) Fe-rich coating; box shows sector depicted in (d). (d) Fe–Co–Ni-rich grain (Table 1).

'Obtusum Claystone' (*Obtususton*) Formation; the Pliensbachian 'Numismalis Marlstone' (*Numismalismergel*) and 'Amaltheus Claystone' (*Amaltheenton*) Formations; as well as the Toarcian 'Posidonia Shale' Formation (*Posidonienschiefer*) and 'Jurensis Marlstone' (*Jurensemergel*) Formation; and the lowermost Middle Jurassic Opalinus Claystone, the iron oolithic Middle Jurassic *Eisensandstein* Formation, as well as the Palaeogene residual deposits of the 'Bohnerz' (bog ore) Formation are the most noticeable sedimentary units with respect to a potentially high concentration of trace metals. The main major elements and the most abundant trace elements for the aforementioned sedimentary units are shown in Figure 11 and listed in Table 4. Vanadium (up to 900 ppm), Sr (up to 1720 ppm), Zr (up to 850 ppm), Cr (up to 240 ppm), Zn (up to 3000 ppm) and Pb (up to 790 ppm) concentrations are remarkably high in these units, whereas Ni, Co, Cu and, in particular, Au concentrations are generally low (below ~0.1 ppm). The Opalinus Claystone is characterized by a typical phyllosilicate mineral geochemistry, usually with high Ti and low Mn concentrations (e.g. Fröhlich *et al*. 2011). Trace elements are dominated by Ba, Sr, Zr, V, Cr, Rb and Zn (Table 4, columns 1 and 2). The composition of the Middle Jurassic Eisensandstein Formation is dominated by quartz and phyllosilicate minerals, and typically contains up to ~43 wt % of iron oxides and oxyhydrates (e.g. Linhardt & Zarbok, 2005). The most abundant trace elements in these predominantly iron oolithic sandstones are V, Cr, Ba, Zn, Sr, Rb and As (see Table 4, column 3). Jurassic black schist-type deposits, as exemplified by the Posidonia Shale, also feature a characteristic phyllosilicate mineral geochemistry, with comparatively high Ca and Ti concentrations and low Mn. The dominant trace elements in the Posidonia black shale are Sr, Zn, Ba, V, Cr, As and Pb (e.g. Brumsack, 1991; Table 4, column 4). Besides having a phyllosilicate mineral geochemistry, the Palaeogene Bohnerz Formation is dominated by high contents of Fe oxides and oxyhydrates (up to ~70 wt %), as well as Mn, P and Ti. The most abundant trace element is Zn, followed by high V, Pb, Zr, Cr, Sr and As concentrations (e.g. Geyer, 1957; Table 4, column 5). In the literature, Au concentrations are usually not listed for these stratigraphic units, presumably because Au concentrations are negligible (<0.1 ppm in the Posidonia Shale; Brumsack, pers. comm. 2014) and, possibly, owing to

https://doi.org/10.1017/S0016756816001357 Published online by Cambridge University Press

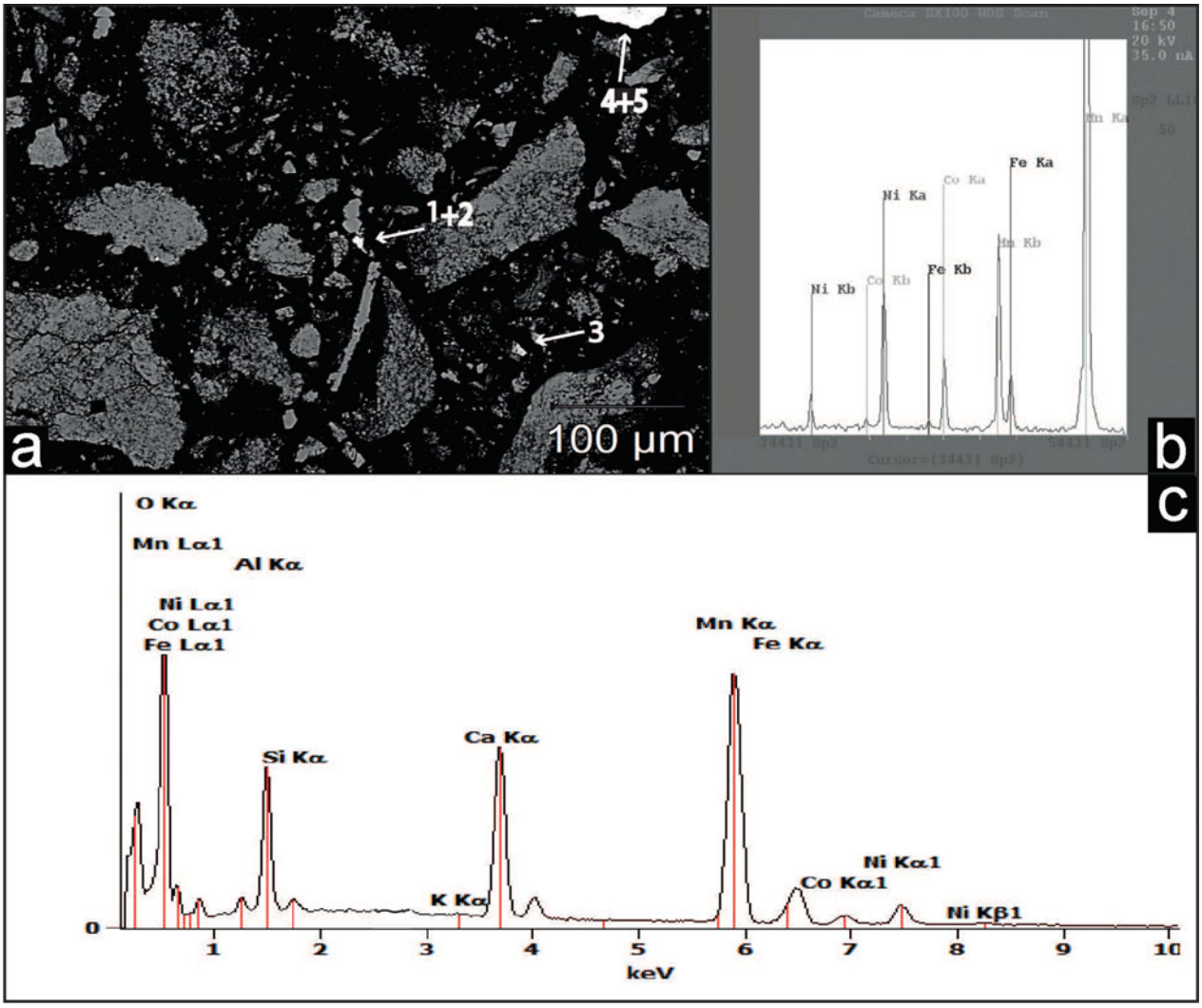

Figure 7. (Colour online) Polished thin-section, with (a) particles of carbonate (light grey) and Mn–Fe–Ni-Co-rich aggregates (white) scraped from the surface of three Upper Jurassic limestone shatter cones (SC-L5), embedded in resin, cut and polished; numbers 1–5 mark locations of EPM analyses. (b, c) Microprobe analyses of Mn–Fe–Ni–Co-rich aggregates (location 1 in (a)), with (b) showing a WDS scan of the crucial sector of the EDS spectrum of Mn, Fe, Ni and Co peak interference.

technical problems in Au detection in X-ray fluorescence analysis.

5.a.2. Contamination from the Palaeozoic crystalline-metamorphic basement?

The Variscan (Moldanubian) crystalline-metamorphic basement in the Steinheim area is covered by a ~1100 m thick suite of sediments (e.g. Stöffler, Artemieva & Pierazzo, 2002). According to Reiff (1992) and Buchner & Schmieder (2015), the transient crater of the Steinheim Basin possibly reached a depth of 1200 m and, thus, may have affected the uppermost portion of the basement. However, as all shatter cones analysed in this study formed in Middle and Upper Jurassic rocks, several hundred metres of Triassic to Lower Jurassic sedimentary rocks would have separated the crystalline-metamorphic basement from the stratigraphic levels of shatter coning (and no shatter cones have so far been reported from the Upper Triassic Keuper sandstones in the Steinheim drill cores; compare, e.g. Heizmann & Reiff, 2002; Buchner & Schmieder, 2010). Moreover, no fragments of Variscan crystalline-metamorphic rocks have been found in the crater-filling impact breccia at Steinheim (e.g. Heizmann & Reiff, 2002). Thus, contamination of the shatter cone surfaces with particulate matter directly derived from the deeper crater basement is unlikely. Theoretically, a post-impact hydrothermal system inside and beneath the Steinheim crater may have dissolved Au and other rare metals from the crystalline-metamorphic rocks in the crater basement. Primary gold mineralization types in the Variscan basement comprise gold-bearing ores in the parageneses Au–Cu–Zn–Pb, Au–As–Bi–Mo–Te–W, and Au–Ag–As and secondary Au mineralization usually contains significant amounts of Cu, Ag, Zn, As, Bi and Pb (A. Schmiderer, unpub. Ph.D. thesis, Univ. Halle-Wittenberg, 2008). Whereas Cu was detected on some shatter cone surfaces and Zn was encountered in a single grain on one limestone shatter cone specimen, Ag, As, Bi and Pb were not detected in any of the

https://doi.org/10.1017/S0016756816001357 Published online by Cambridge University Press

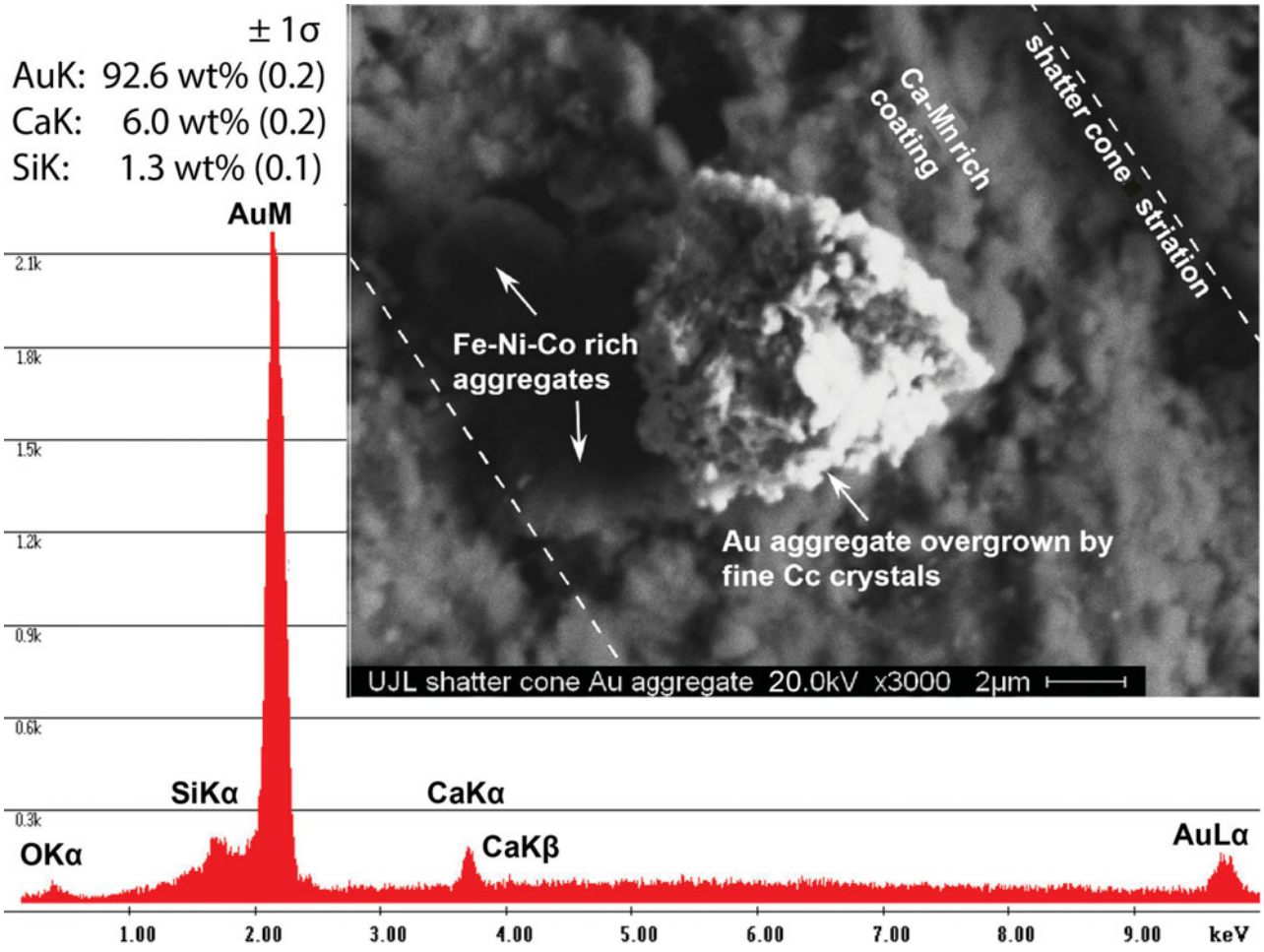

Figure 8. (Colour online) EDS X-ray spectra (15–20 kV) for spots analysed on an Au aggregate embedded in Ca–Mn-rich coating on the surface of an Upper Jurassic limestone shatter cone (SC-L3), as well as the chemical composition of the gold aggregate covered by fine calcite crystals (Cc) and traces of silica. Although Si is quantified as silica and Ca as carbonate (see O peak), Au, Si and Ca abundances are given in element wt %, normalized to 100 %. In addition to this Au aggregate, two roundish Fe–Ni–Co-rich aggregates were encountered.

SEM–EDS analyses carried out in this study. The presence of the elements Au, Ni, Co, Pt and Cu found on the Steinheim shatter cone coatings and the absence of elements such as Ag, Zn, Cr and Pb could theoretically be an effect of the prevailing temperature conditions of the hydrothermal system, or could be caused by fractionation due to differential uptake of different ions in aqueous solutions. According to Zhu, An & Tan (2011), hydrothermal systems without distinct affinities to magmatic activity and relatively low (epithermal) temperatures of ≤300 °C (as expected for the rather small Steinheim Basin that formed in water-saturated, porous target rocks; Buchner & Schmieder, 2013*a*, 2015) would result in the formation of hydrothermal ore deposits that may contain Au and elements such as Ag, Zn, Sb and Pb. From this point of view, it seems rather unlikely to consider the Variscan basement rocks as the source for the rare metals found on the Steinheim shatter cones; however, we cannot entirely exclude this possibility.

5.a.3. Anthropogenic contamination?

The occurrences of rare metals on the shatter cone surfaces might be the result of recent (or subrecent) contamination either in the laboratory or in the field. Hundreds of small aggregates of native gold, as well as dispersed individual Au particles of up to 20 μm in size occur on the surfaces of some shatter cones. As Au is a common contaminant in SEM laboratories that use gold sputters, we cannot definitely rule out that we detected some contaminant Au particles on shatter cone surfaces. However, we interpret the vast majority of the Au particles detected as *in situ* formation for the following reasons: (1) Au particles usually overgrow (or are intergrown with) the shatter cone coatings (SC-C5; compare Fig. 5); (2) many of the Au particles are overgrown by small crystals of calcite (and sometimes silica) and/or by phases of Fe hydroxides or phyllosilicates (compare Figs 8 and 9); (3) the Au particles often represent alloys of Au with Cu, Ni and other metals (Fig. 9). The concentration of Cu in some of the

https://doi.org/10.1017/S0016756816001357 Published online by Cambridge University Press

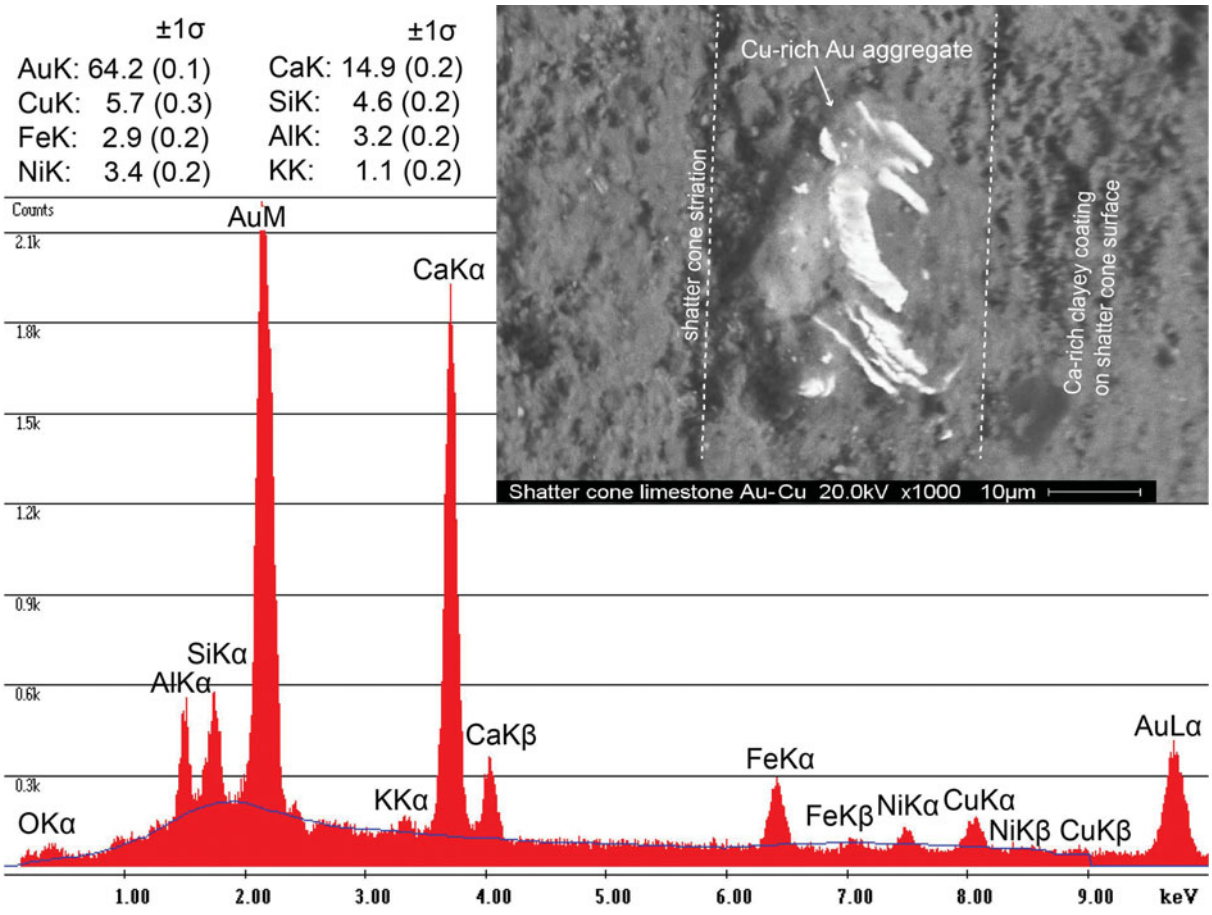

Figure 9. (Colour online) EDS X-ray spectra (15–20 kV) for spots on an Au aggregate embedded in Ca-rich and phyllosilicate (illite) coating on the surface of an Upper Jurassic limestone shatter cone (SC-L3), as well as the chemical composition of the gold aggregate (Au–Cu–Ni alloy) covered by fine calcite crystals and phyllosilicate minerals. Values are given as element wt %, normalized to 100 %.

Au particles locally exceeds several wt %. In remarkable contrast, the purity of the gold targets used in the Stuttgart SEM laboratory is at least 99.99 wt %. To avoid contamination of the shatter cone samples with Au, C or other elements from the sputter apparatus, we carried out additional SEM–EDS analyses on an uncoated specimen of Opalinus Claystone shatter cones (CS-C2) that has a Fe-rich natural coating. On the surface of this shatter cone, we detected the same elements as in the coatings of C-coated shatter cones, in particular, high values of Fe, Ni, Co (quantified as oxides) and some Au particles. Gold contamination from the scalpel can be ruled out because the scalpel, used to mechanically scrape off surface coating material from the shatter cone surfaces for thin-sectioning and EPMA, is composed of Fe, Mn, C and Cr.

Moreover, metallurgical processes in the context of historical bog ore smelting may potentially cause subrecent contamination of shatter cone surfaces with rare metals. According to Geyer (1957), bog ore was mined and smelted in large areas of the Swabian Alb in the Middle Ages; so it was in the greater Steinheim area (e.g. near Heidenheim a. d. Brenz and Königsbronn, only a few kilometres away from the Steinheim Basin). However, the pisolithic Bohnerz and its host clays have been shown to contain only traces of Ni (<500 ppm; Borger & Widdowson, 2001). Moreover, we can widely exclude this type of contamination for the Opalinus Claystone shatter cones because these shatter cones were only recently excavated during water catchment works on top of the Steinheim central uplift in April 2010. Furthermore, we only analysed fresh shatter cone individuals never exposed previously, after breaking the intact shattered Opalinus Claystone nodules.

5.a.4. Possible meteoritic contamination from the Steinheim asteroid?

Alternatively, the rare metals concentrated in the coatings of the Steinheim shatter cones may possibly represent the redistributed geochemical relics of the impacting meteorite that formed the Steinheim Basin, earlier proposed to have been an iron or stony-iron meteorite (Schmieder & Buchner 2009, 2010*b*; Buchner & Schmieder, 2010). The preponderance of Fe, Ni, Co, Cu, S, P and the presence of some resolvable Pt in the shatter cone coatings is compatible with an iron meteorite as the potential source for these elements.

https://doi.org/10.1017/S0016756816001357 Published online by Cambridge University Press

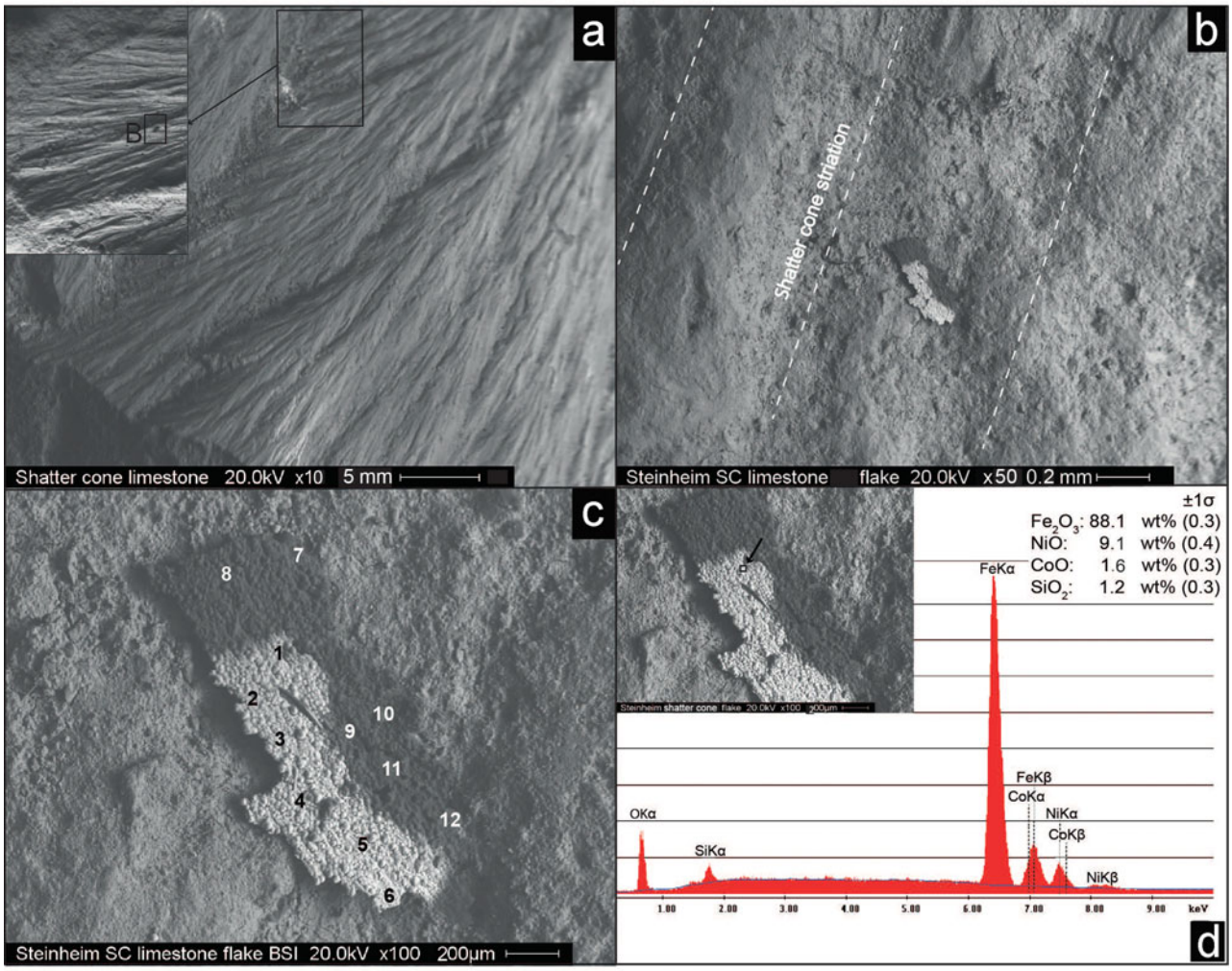

Figure 10. (Colour online) Upper Jurassic limestone shatter cone (SC-L4) surface (a) with a Fe–Ni–Co-rich flake (b–d). The flake shows a botryoidal surface texture and exhibits a brighter (metallic) and a darker (more siliceous) portion. (c) shows locations of the 12 SEM–EDS measurements listed in Table 3. (d) shows a typical EDS X-ray spectra (measurement 1 in image (c)); element values in oxide wt %, normalized to 100 %.

The geochemistry of the different types of meteorites is dominated either by silicate minerals in achondrites and chondrites, or by Fe, S, P, Ni and Co in iron meteorites and/or in the metallic portion of stony-iron meteorites. Among the trace elements, Ge, Ga and Cu play a key role. The Au content in achondrites and chondrites is usually very low, whereas stony-iron and, in particular, iron meteorites typically have much higher Au concentrations (e.g. Danielson, Righter & Humayun, 2009; see Table 5) of >5 ppm (Bauer & Schaudy, 1970) and in some cases as high as >18 ppm (Hecht & Fenninger, 1963). For a compilation of the Au concentration in representative meteorites of different types, see Table 5. Iron and stony-iron meteorites contain Fe, Ni and Co in the per cent range, while Cu is usually the most abundant trace element (e.g. Smales, Mapper & Fouché, 1967; Bauer & Schaudy 1970; Wolf, Wang & Lipschutz, 2009).

The Opalinus Claystone shatter cone (SC-C3) contains relatively high Pt concentrations (≤1.45 wt % PtO, see Table 1). According to, for example, Pernicka & Wasson (1987) and Tagle & Hecht (2006), Pt is also abundant in iron meteorites. Platinum group element (PGE) ratios have been traditionally used to discriminate between different types of meteorites and to investigate meteoritic contamination (e.g. Evans, Gregoire & Goodfellow, 1993; Koeberl 1998, 2014; Goderis, Paquay & Claeys 2012). However, although Fe, P, S, Ni and Co concentrations in the coatings on the surfaces of the Opalinus Claystone shatter cones are rather high, they usually do not occur in proportions typical for minerals in iron meteorites (e.g. the Fe–Ni metal phases kamacite or taenite). Thus, these coatings are unlikely to represent primary remnants of the supposedly iron meteoritic Steinheim impactor (compare Schmieder & Buchner, 2009, 2010*b*; Buchner & Schmieder, 2010 and discussion of possible impactor signatures therein). For a summary of the characteristics and composition of Opalinus Claystone shatter cone coatings see Table 6, SC-C1 to SC-C6).

https://doi.org/10.1017/S0016756816001357 Published online by Cambridge University Press

Table 4. X-ray fluorescence (XRF) analyses of main and trace elements (bulk analyses) of the Middle Jurassic Opalinus Claystone, Lower Jurassic Posidonia Shale, Middle Jurassic Eisensandstein Formation and Palaeogene Bohnerz Formation taken from the literature

Column	1	2	3	4	5
Elements	Opalinus Clay, XRF data;Fröhlich *et al*. (2011) Ø of 5 analyses	Opalinus Clay, XRF data; Fröhlich *et al*. (2012)	Eisensandstein Formation, XRF data; Linhardt & Zarbok (2005)	Posidonia Shale, XRF data; Brumsack (1991) Ø of 4 analyses	Bohnerz Formation, Roller (1904), compilation of XRF data in Geyer (1957) and NTB 88-11 (1992)
			Major elements, wt %		
Si	42.62	47.7	26.1–31.9	27.2	10-30
Al	18.81	19.2	0.84–5.00	7.9	15–20
Fe	5.61	7.7	2.74–42.70	4.52	50–70
Ca	9.10	4.1	0.04–13.73	20.9	~2
K	2.79	2.9	0.10–1.12	1.51	2–3
Mg	2.15	2.2	0.18–0.60	0.04	0–1
S	1.26	0.5	0.40–2.99	2.93	~0.4
Mn	0.05	0.1	0.004–0.16	0.07	~2–3
Na	0.28	0.4	0.02–0.05	0.28	0-0.5
P	0.22	0.3	0.04–0.54	0.25	~2
Ti	0.80	0.9	0.04–0.63	0.38	~1
			Trace elements, ppm		
V	151	170	15–268	163	900
Sr	235	284	10–90	1720	210
Zr	147	173			850
Cr	136	138	17–239	65	240
Rb	128	121	0.43–93		
Zn	124	89	1–107	285	up to 3000
Ba	295	288	38–179	191	
Pb				23	790
As			3–68	28	120

For Opalinus Claystone, Posidonia Shale, Eisensandstein Formation and Bohnerz Formation, the seven most abundant trace elements are listed.

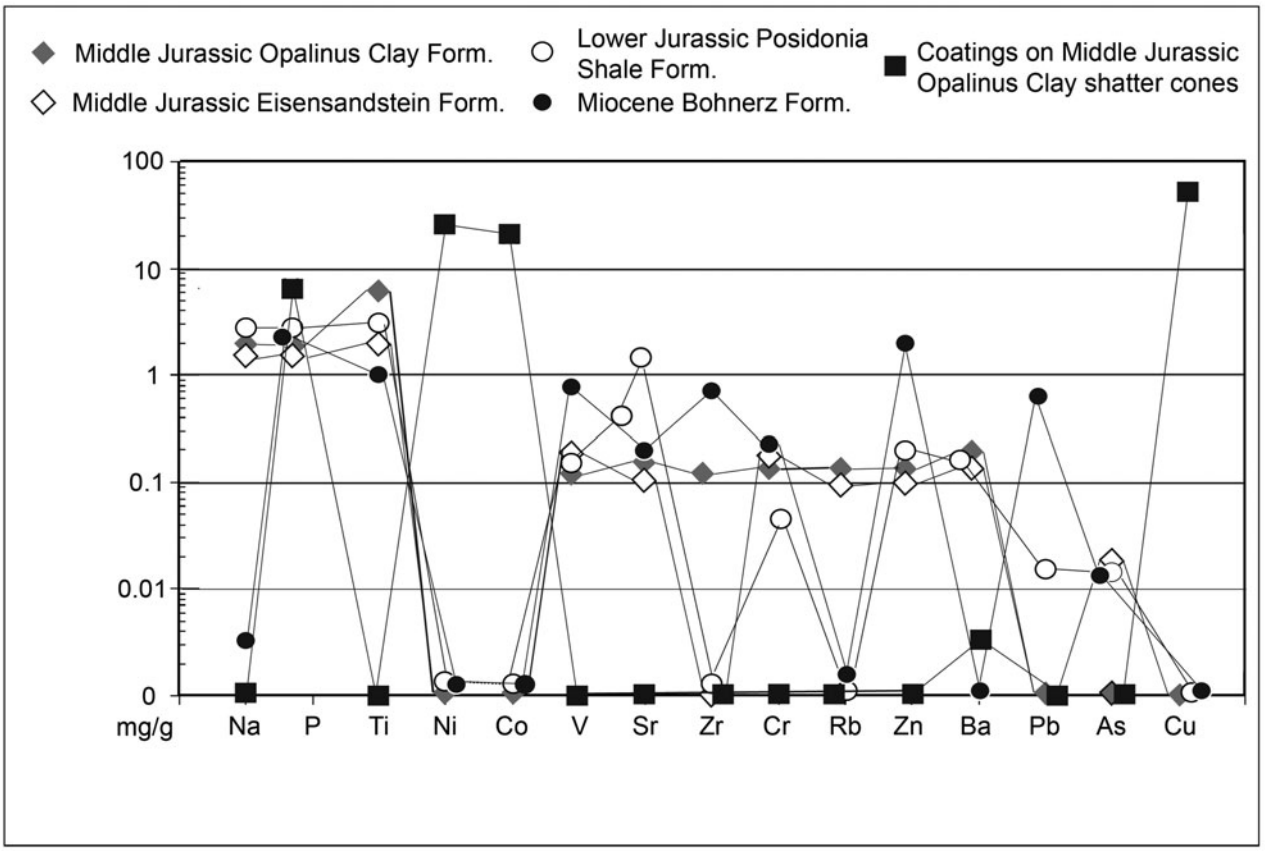

Figure 11. Geochemical data for the shatter cone coatings plotted against the data of the sedimentary target rocks (compare to Table 4). The overall trend of the geochemical signature of the shatter cone coatings runs contrary to the geochemical signature of the sedimentary target rocks.

https://doi.org/10.1017/S0016756816001357 Published online by Cambridge University Press

Table 5. Au concentration (ppm) of some representative meteorites in different meteorite classes. The bulk Au concentration systematically increases from achondrites to iron meteorites

Meteorite classification	Denomination of samples and meteorite groups							Literature
Achondrites	Allende range of three analyses	Moon meteorites range of 14 meteorites analysed	Mars meteorite DaG 476	Ungrouped Achondrite, QUE 93148 metallic portion*	Achondrite (Ca-rich) average of 8 meteorites**	Achondrite (Ca-poor) average of 8 meteorites**		Wolf *et al*. (2009) *Korotchantseva *et al*. (2003) **Jones (1968)
Au concentration (ppm)	0.193–0.146	0000.17–0.024	00.105	0.985	0.014	0.0037		
C-type chondrites	Efremovka (CV3 chondrite)	Orgueil (C1 chondrite)*	Essebi (C2M chondrite)*	Murchison C2M chondrite*	CI chondrite mean**	C-type chondrite average of 8 meteorites**		Krot *et al*. (1999) *Xiao & Lipschutz (1992) **Anders (1988)
Au concentration (ppm)	0.167–0.228	0.145	0.136	0.149	0.14	0.16		
Ordinary chondrites	Wuan (H6 chondrite)	Zaoyang (H5 chondrite)	Zhadong (L4 chondrite)	Laocheng (H5 chondrite)	Changxing (H5 chondrite)	Mocs (L6 chondrite)*	Chondrites average of 24 meteorites**	Chen, Wang & Pernicka (1992) *Hecht & Fenninger (1963) **Jones (1968)
Au concentration (ppm)	1.17	1.14	1.64	0.985	0.864	0.3	0.21	
Stony-iron meteorites	Mesosiderite RKPA 79015 bulk analysis	Mesosiderite RKPA 79015 analysis of kamacite	Mesosiderite RKPA 79015 analysis of taenite	Pallasite Cumulus Ridge (CMS) 04071 bulk metal*	Pallasite Cumulus Ridge (CMS) 04071 kamacite*	Pallasite Cumulus Ridge (CMS) 04071 taenite*	Stony-iron meteorites average of 8 meteorites**	Korotchantseva *et al*. (2003) *Danielson, Righter & Humayun (2009) **Jones (1968)
Au concentration (ppm)	1.5	4.45	1.21	3.58	2.77	5.48	1.5	
Iron meteorites	IAB range of six meteorites analysed	IIAB range of six meteorites analysed	IID range of six meteorites analysed	IIIAB range of nine meteorites analysed	IIICD range of nine meteorites analysed	IIIF range of five meteorites analysed	Ataxites range of 25 meteorites*	Pernicka & Wasson (1987) *Jones (1968)
Au concentration (ppm)	1.33–1.74	0.46–0.97	0.52–1.35	0.43–2.43	1.31–1.73	0.265–2.87	1.2–2.9	
Iron meteorites	Magura (IAB)	San Cristobal IB	Wallapai (IID)*	Canyon Diablo (IA)*	Colomera (IIE)*	Hexahedrites range of 107 meteorites**		Bauer & Schaudy (1970) *Hsu, Huss & Wasserburg (2000) **Jones (1968)
Au concentration (ppm)	3.9	2.5	3.5	4.2	5.7	1.8–4.7		

Note that the metallic portions of achondrites, chondrites and stony-iron meteorites also contain high amounts of Au.

Table 6. Compilation of the characteristic properties of all claystone and limestone shatter cones investigated in this study

Abbreviations of shatter cone samples used in text and tables	Type of sample	Sizes of shatter cone samples	Overall appearance of shatter cone surface and characterization of shatter cone coating	Method and number of analyses	Elements detected in coatings
SC-C1	Shatter cone individual taken from a shattered Middle Jurassic Opalinus Claystone nodule	*c.* 1 cm	Yellowish to brown; bright, shiny coating on the entire shatter cone surface	SEM–EDS; carbon coated; ten analyses of optically bright areas in BSE mode (Table 1)	– Mainly oxides – Fe-rich coating (*c.* 75 wt % Fe_2O_3) with traces of NiO and CoO; CuO significantly enriched in nearly all analyses; few barite aggregates – Finely dispersed micro-grains of Au; grains visible in BSE mode but grain sizes are below spot size
SC-C2	Shatter cone individual taken from a shattered Middle Jurassic Opalinus Claystone nodule	*c.* 1.5 cm	Dark brown; dark patches on shatter cone surface	SEM–EDS; not carbon coated; ten analyses of patches (Table 1)	– Oxides – Fe-rich patches (*c.* 95 wt % Fe_2O_3); NiO and CoO enriched – Finely dispersed micro-grains of Au; grains are visible in BSE mode but grain sizes are below spot size
SC-C3	Shatter cone individual taken from a shattered Middle Jurassic Opalinus Claystone nodule	*c.* 1.5 cm	Light brown; aggregates randomly distributed on shatter cone surface	SEM–EDS; carbon coated; ten analyses of metallic aggregates (Table 1)	– Oxides – Aggregates rich in Fe_2O_3, SiO_2, Al_2O_3, K_2O and CaO; NiO and CoO significantly enriched; PtO significantly enriched in two metallic aggregates – Finely dispersed micro-grains of Au; grains are visible in BSE mode but grain sizes are below spot size
SC-C4	Shatter cone individual taken from a shattered Middle Jurassic Opalinus Claystone nodule	*c.* 1.5 cm	Yellow; bright, shiny coating on entire shatter cone surface	SEM–EDS; carbon coated; ten analyses of optically bright areas in BSE mode (Table 1)	– Sulfates and oxides – Many barite aggregates and Fe-rich coating, NiO and CoO slightly enriched – Finely dispersed micro-grains of Au; grains are visible in BSE mode but grain sizes are below spot size
SC-C5	Shatter cone individual taken from a shattered Middle Jurassic Opalinus Claystone nodule	*c.* 3 cm	Dark brown; dark patches on shatter cone surface	SEM–EDS; carbon coated; six analyses of patches (Table 1)	– Oxides – Fe-rich patches (*c.* 88 wt % Fe_2O_3); NiO and, in particular, CoO strongly enriched – Many fine aggregates of Au, up to 20 μm in size
SC-C6	Two thin-sections; particles scraped from the surfaces of three Middle Jurassic Opalinus Claystone shatter cone individuals	Shatter cones of varying sizes	Coatings of varying appearance	EPMA; carbon coated; three analyses of selected metallic aggregates (Table 1)	– Oxides – Coating rich in Fe, S, Al, Ca, Mn and P; Ni and Co significantly enriched; Cu enriched

Table 6. Continued

Abbreviations of shatter cone samples used in text and tables	Type of sample	Sizes of shatter cone samples	Overall appearance of shatter cone surface and characterization of shatter cone coating	Method and number of analyses	Elements detected in coatings
SC-L1	Upper Jurassic limestone shatter cone	*c.* 4 cm	Brownish to red; dark patches on shatter cone surface	SEM–EDS; carbon coated; 15 analyses of optically bright areas in BSE mode (Table 2)	– Oxides – Coating rich in CaO and MnO – Patches rich in Fe_2O_3, NiO and CoO – Finely dispersed micro-grains of Au; grains are visible in BSE mode but grain sizes are below spot size
SC-L2	Upper Jurassic limestone shatter cone	*c.* 4 cm	Brownish to red; dark patches on shatter cone surface	SEM–EDS; carbon coated; 14 analyses of optically bright areas in BSE mode (Table 2)	– Oxides – Coating rich in CaO and MnO – Patches rich in Fe_2O_3, NiO and CoO – Finely dispersed micro-grains of Au; grains are visible in BSE mode but grain sizes are below spot size
SC-L3	Upper Jurassic limestone shatter cone	*c.* 5 cm	Greenish to grey; many aggregates randomly distributed on shatter cone surface	SEM–EDS; carbon coated; 15 analyses of metallic aggregates (Table 2)	– Mainly oxides – Aggregates rich in Fe_2O_3, NiO and CoO; two aggregates rich in Cu; one large barite aggregate; one aggregate rich in Zn – Many fine aggregates of Au, up to 20 μm in size
SC-L4	Upper Jurassic limestone shatter cone	*c.* 6 cm	Light grey; one flake analysed (flake consists of a dark and a bright portion)	SEM–EDS; carbon coated; 12 analyses, six of bright and six of dark portion of flake (Table 3)	– Oxides – Dark portion of flake rich in SiO_2, Al_2O_3, CaO, MgO and Fe_2O_2; NiO and CoO significantly enriched in all analyses; CuO, PtO, GeO_2 and Ga_2O_3 significantly enriched in two analyses – Bright portion of flake rich in Fe_2O_3, NiO and CoO; GeO_2 enriched in four analyses; Ga_2O_3 enriched in two analyses; CuO and PtO enriched in one analysis
SC-L5	Two thin-sections; particles scraped from the surfaces of three Upper Jurassic limestone shatter cones	Shatter cones of varying sizes	Coatings of varying appearance	EPMA; carbon coated; five analyses of three selected metallic aggregates (Table 2)	– Oxides – Aggregates rich in Ca and Mn, Fe Ni and Co – Au particles probably present, but grain sizes are below spot size

The composition of the unusual, botryoidal oxide flake on the surface of limestone shatter cone SC-L4 (Tables 3, 6), with elevated concentrations of Fe, Ni, Co, Pt, Ga and Ge (Table 3; given as oxides), also suggests this flake may represent some sort of meteoritic matter. Again, the composition probably does not reflect the primary, but likely altered, element ratios. The average inter-element ratios (Fe/Ni of ∼9.5 and Ni/Co of ∼7.5) are broadly consistent with the respective whole-rock inter-element ratios of iron meteorites (for instance for octahedrites, e.g. Kracher, Willis & Wasson, 1980; Pernicka & Wasson, 1987), in contrast to most chondrites characterized by a whole-rock Ni/Co of ∼20 (e.g. Schmieder & Buchner, 2010*b* and references therein). The chemistry of the 'darker', more silicate-rich, portion of the flake might be comparable to the composition of the silicate part of a stony-iron meteorite (for instance a mesosiderite, e.g. Powell, 1971). Moreover, the apparent concentration of Pt, Ga and Ge is arguably too high as though the host flake could be considered 'original' meteoritic matter. The botryoidal microtexture of the flake's surface, the high element concentrations of the otherwise rare metals Cu, Pt, Ga and Ge, and, finally, the oxidized mineral phases of the flake argue for an (intensely) altered, potentially meteorite-derived fragment. Any original meteoritic matter may have experienced hydrothermal overprint and partial dissolution, and subsequent local precipitation of Cu-, Pt-, Ga- and Ge-rich oxide phases. Although the interpretation of this unusual flake as oxidized impactor matter remains speculative, the recent finding of several schreibersite aggregates on the surface of a limestone shatter cone from the Agoudal impact site in Morocco (Schmieder *et al*. 2015) indicates that shatter cone surfaces may carry both primary and altered meteoritic matter.

In summary, an origin of the shatter cone coatings (or portions of these) as target rock-derived or anthropogenic contamination seems unlikely. As the crucial trace elements (e.g. V, Sr, Zn and Cr) characteristic for the target sediments of the Steinheim Basin and gold-bearing ores in the Variscan crater basement (e.g. Au, Zn, As, Pb) were not encountered in the coatings, we conclude that it is rather unlikely that Ni, Co, Cu and Au were dissolved from the host rocks of the Steinheim Basin impact crater. Owing to the scarcity of detailed information on the trace element concentration in and the lack of information on the Au content of the sedimentary target rocks, we are not able to exclude the upper Steinheim target rocks as a possible source for the rare metals enriched on the shatter cones. The elements concentrated in the shatter cone coatings, however, suggest a general affinity towards a meteoritic source, possibly an iron meteorite. This interpretation is supported by the occurrence of Fe-Ni-Co-sulfides as fragments and droplets in melt particles of the Steinheim Basin impact breccia (Schmieder & Buchner, 2009, 2010*b*) and Fe-Ni-Co spherules adherent to melt particles therein (Buchner & Schmieder, 2009), as well as by the high concentrations of Au and Cu within Fe-sulfide aggregates in the Steinheim breccia (Buchner & Schmieder, 2010, 2013*b*).

5.b. Potential influence of impact-induced hydrothermal activity

One possible way to generate surface coatings on shatter cone fractures in the shocked target rock is the post-impact precipitation of elements from hot fluids that circulate in a hot, cooling impact crater (e.g. Zürcher & Kring, 2004; Naumov, 2005; Osinski *et al*. 2013; Schmieder & Jourdan, 2013). The coatings on the surface of all shatter cones analysed, containing chiefly the same elements in variable proportions, could represent an epigenetic mineralization in response to a hydrothermal system that developed inside the fresh Steinheim impact crater. The existence of a post-impact hydrothermal system in the Steinheim Basin, although probably rather short-lived, is supported by the high water content of weathered melt particles in the Steinheim Basin impact breccia (Buchner & Schmieder, 2010, 2013*b*; Anders *et al*. 2013), which are almost completely altered into phyllosilicates (compare Osinski, 2005; Muttik *et al*. 2008), and the presence of a freshwater carbonate spring mound on the central uplift (the '*Wäldlesfels*'; e.g. Heizmann & Reiff, 2002; Anders *et al*. 2013). Similar to the high water content in the melt particles, the high content of rare metals in framboidal Fe-sulfide aggregates within the Steinheim impact breccia lens (Buchner & Schmieder, 2010, 2013*b*) and in carbonate melt veins (Anders *et al*. 2013) suggests that the post-impact formation of authigenic pyrite may be related to impact-induced hydrothermal activity (e.g. Newsom & Hagerty, 2003). The surfaces of the shatter cones represented open microfractures susceptible to the circulation of hydrothermal solutions, and thereby promoting the precipitation of hydrothermal wall deposits. According to Seward (1991), hydrothermal Au (and other elements, such as Cu and Zn) deposition may occur over a wide temperature, pressure and fluid composition range, and may include lower temperature epithermal mineralization (∼50–300 °C). The circulation of solutions in the early post-impact hydrothermal system at Steinheim likely occurred under such low-temperature conditions. Jõeleht *et al*. (2005) and Versh *et al*. (2005), for example, investigated the hydrothermal system in the ∼4 km in diameter, marine Kärdla impact crater in Estonia in detail. This Ordovician impact crater hosted an impact-induced hydrothermal system in the fractured basement rocks inside its central uplift, and in the surrounding impact breccias. The hydrothermal water–rock interaction in heated impactites is usually characterized by a complex mineralization assemblage. Mineral associations suggest at least three evolutionary stages grad-

https://doi.org/10.1017/S0016756816001357 Published online by Cambridge University Press

ing into one another. A first, vapour-dominated stage of crater cooling was dominated by elevated temperatures exceeding 300 °C; the main cooling stage saw temperatures between ∼300 and 100 °C; and a late liquid-dominated stage was characterized by temperatures below 100 °C. The lowest-temperature stage is associated with the crystallization of late chalcopyrite and pyrite (Versh *et al*. 2005). As a second example, rocks from drill cores into the 1.9 km diameter Lonar crater in India show basaltic impact breccias altered by post-impact hydrothermal processes, and a corresponding assemblage of secondary alteration minerals (Hagerty & Newsom, 2003). Thermodynamic modelling and terrestrial volcanic analogues were used to demonstrate that this mineral assemblage was formed at temperatures as low as ∼130–200 °C. These analogues suggest that the coatings on the shatter cone surfaces of the Steinheim Basin (inside the central uplift, and thus within the structural crater floor) may have been precipitated in the lower, epithermal, temperature range, and that cooling impact craters even smaller than the Steinheim Basin can potentially drive short-lived fluid systems at temperatures sufficient to generate hydrothermal mineral deposits. Numerous barite aggregates associated with one of the Upper Jurassic limestone shatter cones (SC-L3, Table 2) may be examples of secondary, potentially hydrothermally grown or diagenetic, mineral phases.

5.c. Broader significance of 'exotic' shatter cone coatings

Koeberl (1998) pointed out that fragments of the impacting projectile are occasionally preserved in smaller impact craters, whereas in most of the larger craters a smaller amount (mostly <1 %) is mixed in with impact melt rocks or breccias. According to French (1998), most of the impacting projectile is vaporized during a larger impact event. Some rare exceptions in the terrestrial impact cratering record are, for example, the finding of extraterrestrial chromite grains in the resurge breccia of the ≥ 7.5 km diameter Lockne impact structure, Sweden (Alwmark & Schmitz, 2007) and a larger meteorite fragment preserved in the impact melt sheet of the ≥ 70 km Morokweng impact structure, South Africa (Maier *et al*. 2006). Therefore, impactor traces in terrestrial impact structures are usually investigated by the intercorrelation of siderophile elements in impact melt lithologies (e.g. Goderis, Paquay & Claeys, 2012; Koeberl, 2014). The recent report of schreibersite adherent to a shatter cone discovered near Agoudal in Morocco (Schmieder *et al*. 2015) suggests that 'primary' (i.e. largely unaltered) meteoritic material can be preserved in direct association with terrestrial shatter cones, and that shatter cones may hold a significant and underexplored potential in the identification of impactor-derived materials.

The widespread belief that the incoming impactor is completely vaporized in large-scale impacts is not supported by numerical modelling (e.g. Pierazzo & Melosh, 2000). It has been suggested that, at impact angles of <45° and impact velocities of 20 km s^{-1}, less than 50 % of the impactor masses are vaporized, and the remaining fraction is thought to 'survive' the impact process in the form of either melt or as solid aggregates that are eventually deposited within, or down range, of the resultant impact crater (Pierazzo & Melosh, 2000). A splendid terrestrial example for the survival of meteoritic matter in and around an impact crater >1 km in diameter is Meteor Crater in Arizona, USA, generated by the impact of the IA iron meteorite Canyon Diablo (e.g. Blau, Axon & Goldstein, 1973; Kring, 2007). Yue *et al*. (2013) suggested that the projectiles responsible for the formation of large impact structures on the moon are commonly assumed to melt or vaporize during the impact, so that only geochemical traces or small fragments of the impactor remain in the final structure. However, in a numerical simulation of impact crater formation, Yue *et al*. (2013) found that for vertical impact velocities below about 12 km s^{-1}, the projectile may survive the impact and be swept back into the central peak of the final crater as the peak collapses, although the impactor mass would be fragmented and strongly deformed. They concluded that some unusual minerals observed in the central peaks of many lunar impact structures could, thus, represent exogenic meteoritic material.

In analogy to such lunar craters, the central peaks of terrestrial impact craters may be a preferential target for a search for extraterrestrial contamination. Assuming a projectile diameter of ∼150 m and favouring a likely iron meteoritic composition supported by previous geochemical data (Schmieder & Buchner, 2009, 2010*b*), the Steinheim meteorite would have weighed *c*. 14 million tons. According to Jones (1968) and Hsu, Huss & Wasserburg (2000), the average Au content in iron meteorites is about 4 ppm, resulting in a hypothetical estimate of ∼56 t of Au distributed within the incoming Steinheim asteroid. The amount of the impactor mass that survived the Steinheim impact within the impact breccias and as contamination in the target rocks remains speculative. However, the best-fit scenario in the numerical modelling of the formation of the Steinheim Basin suggested an impact velocity of 12 km s^{-1} (Ivanov & Stöffler, 2005) and an impact angle between 30° and 45° (Stöffler, Artemieva & Pierazzo, 2002). According to these results and the modelling by Pierazzo & Melosh (2000) and Yue *et al*. (2013), it seems plausible that the amount of impactor relics in the Steinheim Basin may in fact be surprisingly high, possibly in the order of a few per cent of the original impactor mass. Accordingly, one or more tons of Au may have survived the Steinheim impact event, now intermingled with the Steinheim breccia and as a strongly dispersed particulate contamination of hydrothermally (?) redistributed metals in the rocks of the structural crater floor and inside the central uplift. These possible exogenic Au deposits may have subsequently been dissolved by hot, aqueous hydrothermal solutions and finally been re-precipitated along fluid pathways in the shocked target rocks (such

https://doi.org/10.1017/S0016756816001357 Published online by Cambridge University Press

as shatter cone fractures) and in the porous and, to some degree, permeable impact breccias.

6. Conclusions

This study presents a petrographic and geochemical characterization of shatter cones from the central uplift (Middle Jurassic Opalinus Claystone) and the structural crater floor (Upper Jurassic limestones) of the Steinheim Basin, the surfaces of which are commonly covered by thin coatings. Apart from carbonate and silicate minerals, the coatings are characterized by elevated concentrations of Fe, S, P, Ni, Co, Cu, Pt and Au, mainly distributed within oxidized phases. The variable proportions among these elements are rather atypical for minerals in iron meteorites and, thus, are unlikely to represent the primary remnants of the Steinheim impactor. However, the elements enriched in the shatter cone coatings suggest a general affinity towards an iron meteoritic source, as opposed to the sedimentary target and the underlying crystalline-metamorphic basement rocks that are generally poor in the rare metals encountered. Hundreds of very small aggregates and dispersed micro-grains of native gold occur on the surfaces of several of the shatter cones. A more plausible explanation for the shatter cone coatings is that they might represent redistributed impactor material, potentially remobilized in a hydrothermal system that developed in response to the Steinheim impact. The surfaces of the shatter cones obviously represented open pathways in the form of microfractures in the Steinheim central uplift and crater floor, conducive to the circulation of hydrothermal solutions and the precipitation of post-impact mineral deposits. The Fe-, Ni-, Co-rich composition of an unusual oxide flake on the surface of a limestone shatter cone, with traceable amounts of Cu, Pt, Ga and Ge, also shows a general affinity towards an iron (or stony-iron) meteoritic source. Regardless of their provenance, the occurrence of rare metals on the shatter cone surfaces suggests some degree of hydrothermal mineralization along the shatter cone fractures inside the central uplift and within the crater floor of the Steinheim Basin. This corroborates previous evidence for an impact-induced hydrothermal system that developed inside and beneath this comparatively small, complex impact crater.

Acknowledgements. The authors are grateful to Hans Brumsack (Universität Oldenburg) and Michael Rasser (Naturkundemuseum Stuttgart) for fruitful discussions and helpful hints. We thank Thomas Theye (Institut für Mineralogie und Kristallchemie, Universität Stuttgart) for his help with microprobe analyses and WDS scans, and Moritz Schmelz for thin-section preparation. We want to thank Peter Seidel (Steinheim am Albuch) for providing additional image material. We would also like to thank Paul Buchanan (Kilgore College) and an anonymous reviewer for their helpful suggestions, as well as Editor Chad Deering for handling this manuscript. Bertrand Devouard (Aix-Marseille Université), Marc Biren (University of Arizona) and Birger Schmitz (University of Lund) are thanked for their comments on an earlier version of our manuscript. E.B. acknowledges a grant by the Stifterverband für die Deutsche Wissenschaft. This is LPI Contribution no. 1995.

References

Alwmark, C. & Schmitz, B. 2007. Extraterrestrial chromite in the resurge deposits of the early Late Ordovician Lockne crater, central Sweden. *Earth and Planetary Science Letters* **253**, 291–3.

Andalib, F. 1970. Mineralogisch-geochemische Untersuchungen der aragonitischen Fossilien aus dem Dogger alpha (Opalinuston) in Württemberg. *Arbeiten aus dem Geologisch-Paläontologischen Institut der Universität Stuttgart (TH), Neue Folge* **62**, 66 pp. (in German).

Anders, E. 1988. Circumstellar material in meteorites: noble gases, carbon and nitrogen. In *Meteorites and the Early Solar System* (eds J. F. Kerridge & M. S. Matthews), pp. 927–55. Tucson: University of Arizona Press.

Anders, D., Buchner, E., Schmieder, M. & Kegler, P. 2013. Varietäten von Schmelzelithologien in den Impaktiten des Steinheimer Beckens (SW-Deutschland). *Zeitschrift der Deutschen Gesellschaft für Geowissenschaften (German Journal of Geology)* **164**, 491–501 (in German).

Baratoux, D. & Melosh, H. J. 2003. The formation of shatter cones by shock wave interference during impacting. *Earth and Planetary Science Letters* **216**, 43–54.

Baratoux, D. & Reimold, W. U. 2016. The current state of knowledge about shatter cones: introduction to the special issue. *Meteoritics & Planetary Science* **51**, 1389–34.

Bauer, R. & Schaudy, R. 1970. Activation analytical determination of elements in meteorites, 3. Determination of manganese, sodium, gallium, germanium, copper and gold in 21 iron meteorites and 2 mesosiderites. *Chemical Geology* **6**, 119–31.

Blau, P. J., Axon, H. J. & Goldstein, J. I. 1973. Investigation of the Canyon Diablo metallic spheroids and their relationship to the breakup of the Canyon Diablo meteorite. *Journal of Geophysical Research* **78**, 363–74.

Borger, H. & Widdowson, M. 2001. Indian laterites, and lateritious residues of southern Germany: a petrographic, mineralogical, and geochemical comparison. *Zeitschrift für Geomorphologie, Neue Folge* **45**, 177–200.

Branco, W. & Fraas, E. 1905. Das kryptovulcanische Becken von Steinheim. *Abhandlungen der königlich preussischen Akademie der Wissenschaften zu Berlin. Physikalisch Abhandlungen* **1**, 1–64 (in German).

Brodbeck, M. 1995. Geologie und Hydrogeologie des Blattes 7127 Westhausen (Ostalbkreis). Erläuterungen zur Geologischen Karte 1:25 000. Ph.D. thesis, Institut für Geologie und Paläontologie der Universität Stuttgart, Stuttgart, Germany, 308 pp. (in German). Published thesis.

Brumsack, H.-J. 1991. Inorganic geochemistry of the German 'Posidonia Shale': palaeoenvironmental consequences. In *Modern and Ancient Continental Shelf Anoxia* (eds R. V. Tyson & T. H. Pearson), pp. 353–62. Geological Society of London, Special Publication no. 58.

Buchner, E. & Schmieder, M. 2009. Steinheim Basin impact spherules (abstract #5075). *Meteoritics and Planetary Science* **44**, A44.

Buchner, E. & Schmieder, M. 2010. Steinheim suevite – a first report of melt-bearing impactites from the Steinheim Basin (SW Germany). *Meteoritics and Planetary Science* **45**, 1093–107.

Buchner, E. & Schmieder, M. 2013a. Das Ries-Steinheim-Ereignis – impakt in eine miozäne Seen- und Sumpflandschaft. *Zeitschrift der Deutschen Gesellschaft für Geowissenschaften (German Journal of Geology)* **164**, 459–70.

Buchner, E. & Schmieder, M. 2013b. Der Steinheimer Suevit – schmelzeführende Impaktite aus dem Steinheimer Becken, Südwestdeutschland. *Zeitschrift der Deutschen Gesellschaft für Geowissenschaften (German Journal of Geology)* **164**, 471–90.

Buchner, E. & Schmieder, M. 2015. The Steinheim Basin impact crater (SW-Germany) – where are the ejecta? *Icarus* **250**, 529–43.

Buchner, E. & Schmieder, M. 2016a. Discovery of possible meteoritic matter on shatter cones and slickensides – 1. Ries crater, Southern Germany. *79th Annual Meeting of the Meteoritical Society (7–12 August 2016), Berlin, Germany, abstract no. 6027*.

Buchner, E. & Schmieder, M. 2016b. Discovery of possible meteoritic matter on shatter cones – 2. Clearwater East impact structure, Québec, Canada. *79th Annual Meeting of the Meteoritical Society (7–12 August 7–12 2016), Berlin, Germany, abstract no. 6028*.

Buchner, E., Schwarz, W. H., Schmieder, M. & Trieloff, M. 2010. Establishing a 14.6 ± 0.2 Ma age for the Nördlinger Ries impact (Germany) – a prime example for concordant isotopic ages from various dating materials. *Meteoritics and Planetary Science* **45**, 662–74.

Buchner, E., Schwarz, W. H., Schmieder, M. & Trieloff, M. 2013. Das Alter des Meteoritenkraters Nördlinger Ries – eine Übersicht und kurze Diskussion der neueren Datierungen des Riesimpakts. *Zeitschrift der Deutschen Gesellschaft für Geowissenschaften (German Journal of Geology)* **164**, 433–45.

Chen, Y., Wang, D. & Pernicka, E. 1992. The compositions of six Chinese ordinary chondrites and element distributions in their different phases. *Chinese Journal of Chemistry* **11**, 214–23.

Danielson, L. R., Righter, K. & Humayun, M. 2009. Trace element chemistry of Cumulus Ridge 04071 pallasite with implications for main group pallasites. *Meteoritics and Planetary Science* **44**, 1019–32.

Dietz, R. S. 1959. Shatter cones in cryptoexplosion structures (meteorite impact?). *The Journal of Geology* **67**, 496–505.

Dietz, R. S. 1960. Meteorite impact suggested by shatter cones in rock. *Science* **131**, 1781–84.

Dietz, R. S. & Butler, L. W. 1964. Shatter-cone orientations at Sudbury, Canada. *Nature* **4**, 204–5.

Di Vincenzo, G. & Skála, R. 2009. ^{40}Ar–^{39}Ar laser dating of tektites from the Cheb Basin (Czech Republic): evidence for coevality with moldavites and influence of the dating standard on the age of the Ries impact. *Geochimica et Cosmochimica Acta* **73**, 493–513.

Engelhardt, W. von, Bertsch, W., Stöffler, D., Groschopf, P. & Reiff, W. 1967. Anzeichen für den meteoritischen Ursprung des Beckens von Steinheim. *Die Naturwissenschaften* **54**, 198–99 (in German).

Etzold, A. 1994. *Geologische Karte von Baden-Württemberg 1:25000, 7126 Aalen, Erläuterungen*. Stuttgart: Landesvermessungsamt Baden-Württemberg, 248 pp. (in German).

Evans, N. J., Gregoire, D. C. & Goodfellow, W. D. 1993. Use of platinum-group elements for impactor identification: terrestrial impact craters and Cretaceous–Tertiary boundary. *Geochimica et Cosmochimica Acta* **57**, 3737–48.

French, B. M. 1998. *Traces of Catastrophe: A Handbook of Shock-Metamorphic Effects in Terrestrial Meteorite Impact Structures*. LPI Contribution no. 954. Houston, Texas: Lunar and Planetary Institute, 120 pp.

French, B. M. & Koeberl, C. 2010. The convincing identification of terrestrial meteorite impact structures: what works, what doesn't, and why. *Earth-Science Reviews* **98**, 123–70.

French, B. M. & Short, N. M. 1968. *Shock Metamorphism of Natural Materials*. Baltimore, Maryland, USA: Mono Book, 644 p.

Fröhlich, D. R., Amayri, S., Drebert, J., Grolimund, D., Huth, J., Kaplan, U., Krause, J. & Reich, T. 2012. Speciation of Np(V) uptake by Opalinus Clay using synchrotron microbeam techniques. *Analytical and Bioanalytical Chemistry* **404**, 2151–62.

Fröhlich, D. R., Amayri, S., Drebert, J. & Reich, T. 2011. Sorption of neptunium(V) on Opalinus Clay under aerobic/anaerobic conditions. *Radiochimica Acta* **99**, 71–7.

Gay, N. C. 1976. Spherules on shatter cone surfaces from the Vredefort Structure, South Africa. *Science* **194**, 724–25.

Gay, N. C., Comins, N. R. & Simpson, C. 1978. The composition of spherules and other features on shatter cone surfaces from the Vredefort structure, South Africa. *Earth and Planetary Science Letters* **41**, 372–80.

Geyer, O. F. 1957. Über das Bohnerz in Württemberg. *Zeitschrift der Deutschen Gesellschaft für Geowissenschaften (German Journal of Geology)* **109**, 22–7.

Geyer, O. F. & Gwinner, M. P. 1991. *Geologie von Baden-Württemberg*. Stuttgart: Schweizerbart-Verlag, 482 pp (in German).

Gibson, H. M. & Spray, J. G. 1998. Shock-induced melting and vaporization of shatter cone surfaces: evidence from the Sudbury impact structure. *Meteoritics and Planetary Science* **33**, 329–36.

Goderis, S., Paquay, F. & Claeys, Ph. 2012. Projectile identification in terrestrial impact structures and ejecta material. In *Impact Cratering: Processes and Products* (eds G. R. Osinski & E. Pierazzo), pp. 223–39. Chichester/Hoboken: Wiley-Blackwell.

Grieve, R. A. F., Palme, H. & Plant, A. G. 1980. Siderophile-rich particles in the melt rocks at the E. Clearwater impact structure, Quebec: their characteristics and relationship to the impacting body. *Contributions to Mineralogy and Petrology* **75**, 187–98.

Groschopf, P. & Reiff, W. 1966. Ergebnisse neuerer Untersuchungen im Steinheimer Becken (Württemberg). *Jahreshefte des Vereins für vaterländische Naturkunde in Württemberg* **121**, 155–68 (in German).

Groschopf, P. & Reiff, W. 1969. Das Steinheimer Becken. Ein Vergleich mit dem Ries. *Geologica Bavarica* **61**, 400–12 (in German).

Hagerty, J. J. & Newsom, H. E. 2003. Hydrothermal alteration at the Lonar Lake impact structure, India: implications for impact cratering on Mars. *Meteoritics and Planetary Science* **38**, 365–81.

Hecht, F. & Fenninger, H. 1963. Determination of trace elements in meteorites. *Progress in Oceanography* **3**, 145–8.

Heitzmann, P. & Bossart, P. 2001. Das Mont-Terri-Projekt. Untersuchungen über den Opalinuston im internationalen Felslabor. *Bulletin für angewandte Geologie* **6**, 183–97 (in German).

Heizmann, E. P. J. & Reiff, W. 2002. *Der Steinheimer Meteorkrater*. Munich: Pfeil-Verlag, 160 pp. (in German).

Hsu, W., Huss, G. R. & Wasserburg, G. J. 2000. Ion probe measurements of Os, Ir, Pt, and Au in individual phases of iron meteorites. *Geochimica et Cosmochimica Acta* **64**, 1133–47

Hüttner, R. & Schmidt-Kaler, H. 1999. *Meteoritenkrater Nördlinger Ries*. Munich: Pfeil-Verlag, 144 pp. (in German).

Ivanov, B. A. & Stöffler, D. 2005. The Steinheim impact crater, Germany: modeling of a complex crater with central uplift. *36th Lunar and Planetary Science Conference, Houston, Texas, USA, 14–18 March 2005, abstract no. 1443.*

Jõeleht, A., Kirsimäe, K., Plado, J., Versh, E. & Ivanov, B. A. 2005. Cooling of the Kärdla impact crater: II. impact and geothermal modeling. *Meteoritics and Planetary Science* **40**, 21–33.

Jones, R. S. 1968. Gold in meteorites and in the Earth's crust. Geological Survey Circular no. 603, 4 pp. US Geological Survey.

Kobler, H.-U. 1972. Geochemische, sedimentologische und ökologische Untersuchungen im Braunen Jura alpha (Opalinuston) der Schwäbischen Alb. *Arbeiten aus dem Geologisch-Paläontologischen Institut der Universität Stuttgart (TH), Neue Folge* **66**, 134 pp. (in German).

Koeberl, C. 1998. Identification of meteoritic components in impactites. In *Meteorites: Flux with Time and Impact Effects* (eds M. M Grady, R. Hutchison, G. H. McGall & D. A. Rothery), pp. 133–53. Geological Society of London, Special Publication no. 140.

Koeberl, C. 2014. Chapter 2.5 – The geochemistry and cosmochemistry of impacts. In *Treatise on Geochemistry, Vol. 2, 2nd ed*. (eds H. D. Holland & K. K. Turekian), pp. 73–118. Amsterdam, New York: Elsevier.

Korotchantseva, E. V., Ivanova, M. A., Lorenz, C. A., Buikin, A. I., Trieloff, M., Nazarov, M. A., Promprated, P. A. & Taylor, L. A. 2003. Major and trace element chemistry and Ar–Ar age of the NWA 011 achondrite. *34th Lunar and Planetary Science Conference, Houston, Texas, USA, 17–21 March 2003, abstract no. 1575*.

Kracher, A., Willis, J. & Wasson, J. T. 1980. Chemical classification of iron meteorites-IX. A new group (IIF), revision of IAB and IIICD, and data on 57 additional irons. *Geochimica et Cosmochimica Acta* **44**, 773–87.

Kring, D. A. 2007. *Guidebook to the Geology of Barringer Meteorite Crater, Arizona (a.k.a. Meteor Crater)*. LPI Contribution no. 1355. Houston, Texas: Lunar and Planetary Institute, 150 pp.

Krot, A. N., Meibom, A., Weisberg, M. K. & Keil, K. 1999. The CR chondrite clan: implications for early solar system processes. *Meteoritics and Planetary Science* **37**, 1451–90.

Langenhorst, F. 2002. Shock metamorphism of some minerals: basic introduction and microstructural observations. *Bulletin of the Czech Geological Survey* **77**, 265–82.

Linhardt, E. & Zarbok, P. 2005. Geochemischer Atlas natürlicher Haupt-, Neben- und Spurenelemente der Gesteine Bayerns. *Bayerisches Landesamt für Umwelt, Fachbericht* **24**, 188 pp. (in German).

Lorenz, C. A., Ivanova, M. A., Artemieva, N. A., Sadilenko, D. A., Chennaoui Aoudjehane, H., Roschina, I. A., Korochantsev, A. V. & Humayun, M. 2014. Formation of a small impact structure discovered within the Agoudal meteorite strewn field, Morocco. *Meteoritics and Planetary Science* **50**, 112–34.

Maier, W. D., Andreoli, M. A. G., McDonald, I., Higgins, M. D., Boyce, A. J., Shukolyukov, A., Lugmair, G. W., Ashwal, L. D., Gräser, P., Ripley, E. M. & Hart, R. J. 2006. Discovery of a 25-cm asteroid clast in the giant Morokweng impact crater, South Africa. *Nature* **441**, 203–6.

Mattmüller, C. R. 1994. *Ries und Steinheimer Becken. Geologischer Führer und Einführung in die Meteoritenkunde*. Stuttgart: Ferdinand Enke Verlag, 152 pp. (in German).

Muttik, N., Kirsimäe, K., Somelar, P. & Osinski, G. R. 2008. Post-impact alteration of surficial suevites in Ries crater, Germany: hydrothermal modification or weathering processes? *Meteoritics and Planetary Science* **43**, 1827–40.

Naumov, M. V. 2005. Principal features of impact-generated hydrothermal circulation systems: mineralogical and geochemical evidence. *Geofluids* **5**, 165–84

Newsom, H. E. & Hagerty, J. J. 2003. Limits of the presence of impact-induced hydrothermal alteration in small impact craters on the Earth: implications for the importance of small craters on Mars. *Impact Cratering: Bridging the Gap between Modeling and Observations. Workshop on Impact Cratering, 7–9 February 2003, Houston, Texas, USA, abstract no. 8049*, p. 51.

Nicolaysen, L. O. & Reimold, W. U. 1999. Vredefort shatter cones revisited. *Journal of Geophysical Research* **104**, 4911–30

NTB 88-11. 1992. Nagra Technischer Bericht 88-11. Sonderbohrung Schafisheim. Untersuchungsbericht. Beilagenband. Nationale Genossenschaft für die Lagerung radioaktiver Abfälle (in German).

Osinski, G. R. 2005. Hydrothermal activity associated with the Ries impact event, Germany. *Geofluids* **5**, 202–20.

Osinski, G. R. & Ferrière, L. 2016. Shatter cones: (mis)understood? *Science Advances* **2**, e1600616, 9 pp. doi: 10.1126/sciadv.1600616.

Osinski, G. R., Tornabene, L. L., Banerjee, N. R., Cockell, C. S., Flemming, R., Izawa, M. R. M., McCutcheon, J., Parnell, J., Preston, L. J., Pickersgill, A. E., Pontefract, A., Sapers, H. M. & Southam, G. 2013. Impact-generated hydrothermal systems on Earth and Mars. *Icarus* **224**, 347–63.

Pernicka, E. & Wasson, J. T. 1987. Ru, Re, OS, Pt and Au in iron meteorites. *Geochimica et Cosmochimica Acta* **51**, 1717–26.

Pierazzo, E. & Melosh, H. J. 2000. Hydrocode modeling of oblique impacts: the fate of the projectile. *Meteoritics and Planetary Science* **35**, 117–30.

Powell, B. N. 1971. Petrology and chemistry of mesosiderites-II. Silicate textures and compositions and metal-silicate relationships. *Geochimica et Cosmochimica Acta* **35**, 5–34.

Reiff, W. 1976. The Steinheim Basin – a meteorite crater. *Abstract Presented at the Symposium on Planetary Cratering Mechanics (13–17 September 1976, Flagstaff, Arizona, USA)*. LPI Contribution no. 259, pp. 112–14.

Reiff, W. 1977. The Steinheim Basin – an impact structure. In *Impact and Explosion Cratering: Planetary and Terrestrial Implications; Proceedings of the Symposium on Planetary Cratering Mechanics, Flagstaff, Arizona, 13–17 September 1976* (eds D. J. Roddy, R. O. Pepin & R. Merrill), pp. 309–20. New York: Pergamon Press.

Reiff, W. 1988. Zur Gleichaltrigkeit der Einschlagskrater (Meteorkrater) Steinheimer Becken und Nördlinger Ries. *Jahresberichte und Mitteilungen des oberrheinischen geologischen Vereins* **70**, 383–97 (in German).

Reiff, W. 1992. Einschlagkrater kosmischer Körper auf der Erde. *Stuttgarter Beiträge zur Naturkunde C* **6**, 24–47 (in German).

Reiff, W. 2004. *Geologische Karte von Baden-Württemberg 1:25000, 7326 Heidenheim, mit Erläuterungen*. Baden-Württemberg: Landesamt für Geologie, Rohstoffe und Bergbau, 223 pp. (in German).

Roller, L. 1904. *Die Bohnerzformation. Oder das Bohnerz und seine Entstehungsweise*. Habilitationsschrift am Polytechnikum Zürich, 162 pp. (in German).

Sagy, A., Fineberg, J. & Reches, Z. 2004. Shatter cones: branched, rapid fractures formed by shock impact. *Journal of Geophysical Research* **109**, 1–20.

Sagy, A., Reches, Z. & Fineberg, J. 2002. Dynamic fracture by large extraterrestrial impacts as the origin of shatter cones. *Nature* **418**, 310–13.

Schmieder, M. & Buchner, E. 2009. Fe-Ni-Co sulfides from the Steinheim Basin, SW Germany: possible impactor traces (abstract #5073). *Meteoritics and Planetary Science* **44**, A185.

Schmieder, M. & Buchner, E. 2010a. New insights into the Steinheim central uplift – part III: shatter cones and the 'cone-in-cone' problem reloaded. *73rd Annual Meeting of the Meteoritical Society (26–30 July 2010), New York, USA, abstract no. 5012*.

Schmieder, M. & Buchner, E. 2010b: Possible iron meteoritic contamination in impact melt particles from the Steinheim Basin (Baden-Württemberg, Germany). *41st Lunar and Planetary Science Conference (1–5 March, 2010), The Woodlands, Texas, USA, abstract no. 2103*.

Schmieder, M. & Buchner, E. 2013. Strahlenkegel in Opalinuston-Konkretionen des Steinheimer Beckens (Baden-Württemberg). *Zeitschrift der Deutschen Gesellschaft für Geowissenschaften (German Journal of Geology)* **164**, 503–13.

Schmieder, M. & Buchner, E. 2016. Discovery of possible meteoritic matter on shatter cones – 3. Marquez Dome, Texas, USA. *79th Annual Meeting of the Meteoritical Society (7–12 August 2016), Berlin, Germany, abstract no. 6029*.

Schmieder, M., Chennaoui Aoudjehane, H., Buchner, E. & Tohver, E. 2015. Meteorite traces on a shatter cone surface from the Agoudal impact site, Morocco. *Geological Magazine* **152**, 751–57.

Schmieder, M. & Jourdan, F. 2013. The Lappajärvi impact structure (Finland): age, duration of crater cooling, and implications for early life. *Geochimica et Cosmochimica Acta* **112**, 321–39.

Schmieder, M., Trieloff, M., Schwarz, W. H., Buchner, E. & Jourdan, F. 2014. Supportive comment on: Morphology and population of binary asteroid impact craters by Miljković, K., Collins, G.S., Mannick, S., and Bland, P. A. 2013 [Earth Planet. Sci. Lett. 363:121–132]. *Earth and Planetary Science Letters* **405**, 281–84.

Selles-Martinez, J. 1994. New insights into the origin of cone-in-cone structures. *Carbonates and Evaporites* **9**, 172–86.

Seward, T. M. 1991. The hydrothermal geochemistry of gold. In *Gold Metallogeny and Exploration* (ed. P. R. Foster), pp. 37–62. Glasgow: Blackie.

Sharpton, V. L., Dressler, B. O., Herrick, R. R., Schnieders, B. & Scott, J. 1996. New constraints on the Slate islands impact structure, Ontario, Canada. *Geology* **24**, 851–54.

Smales, A. A., Mapper, D. & Fouché, K. F. 1967. The distribution of some trace elements in iron meteorites, as determined by neutron activation. *Geochimica et Cosmochimica Acta* **31**, 673–88.

Stöffler, D., Artemieva, N. A. & Pierazzo, E. 2002. Modeling the Ries-Steinheim impact event and the formation of the moldavite strewn field. *Meteoritics and Planetary Science* **37**, 1893–907.

Tagle, R. & Hecht, L. 2006. Geochemical identification of projectiles in impact rocks. *Meteoritics and Planetary Science* **41**, 1721–35.

Versh, E., Kirsimäe, K., Jõeleht, A. & Plado, J. 2005. Cooling of the Kärdla impact crater: I. The mineral paragenetic sequence observation. *Meteoritics and Planetary Science* **40**, 3–19.

Wolf, S. F., Wang, M.-S. & Lipschutz, M. E. 2009. Labile trace elements in basaltic achondrites: can they distinguish between meteorites from the Moon, Mars, and V-type asteroids? *Meteoritics and Planetary Science* **44**, 891–903.

Xiao, X. & Lipschutz, M. E. 1992. Labile trace elements in carbonaceous chondrites: a survey. *Journal of Geophysical Research: Planets* **97**, 10199–211.

Yue, Z., Johnson, B. C., Minton, D. A., Melosh, H. J., Di, K., Hu, W. & Liu, Y. 2013. Projectile remnants in central peaks of lunar impact craters. *Nature Geoscience* **6**, 435–37.

Zhu, Y., An, F. & Tan, J. 2011. Geochemistry of hydrothermal gold deposits: a review. *Geoscience Frontiers* **3**, 367–74.

Zürcher, L. & Kring, D. A. 2004. Hydrothermal alteration in the core of the Yaxcopoil-1 borehole, Chicxulub impact structure, Mexico. *Meteoritics and Planetary Science* **39**, 1199–221.